MAX-PLANCK-INSTITUT FÜR PHYSIK

WERNER-HEISENBERG-INSTITUT

MPI-PhE/93-20
September 1993

TUM–MPI Cryogenic Detector Development 1993

Munich Cryogenic Detector Collaboration

P. Colling[2], S. Cooper[2], D. Dummer[2,*], F.v. Feilitzsch[1], P. Ferger[1], G. Forster[1], M. Frank[2], P. Freund[2], H.-J. Gebauer[2], M. Gutsche[1], K. Hallatschek[1], J. Igalson[2,$], J. Jochum[1], E. Kellner[1], B. Kemmather[1], H. Kraus[1], R.L. Mößbauer[1], U. Nagel[2,&], A. Nowak[2], A. Nucciotti[2], F. Pröbst[2], A. Rulofs[2], W. Seidel[2], L. Stodolsky[2], D. Wilhelm[1]

[1] **Technische Universität München**
Physik-Dept. E15, D-80747 Garching bei München, Germany

[2] **Max-Planck-Institut für Physik**
Föhringer Ring 6, D-80805 München, Germany

* Present Address: Radiometric Physics Division, NIST, Gaithersburg, MD 20899, USA.
$ Permanent Address: Polish Academy of Sciences, Institute of Physics, Warsaw, Poland.
& Permanent Address: Institute of Chemical Physics and Biophysics, Rävala pst. 10, EE0001 Tallinn, Estonia.

TUM–MPI Cryogenic Detector Development 1993

Munich Cryogenic Detector Collaboration

P. Colling[2], S. Cooper[2], D. Dummer[2,*], F.v. Feilitzsch[1], P. Ferger[1], G. Forster[1], M. Frank[2], P. Freund[2], H.-J. Gebauer[2], M. Gutsche[1], K. Hallatschek[1], J. Igalson[2,$], J. Jochum[1], E. Kellner[1], B. Kemmather[1], H. Kraus[1], R.L. Mößbauer[1], U. Nagel[2,&], A. Nowak[2], A. Nucciotti[2], F. Pröbst[2], A. Rulofs[2], W. Seidel[2], L. Stodolsky[2], D. Wilhelm[1]

[1] **Technische Universität München**
Physik-Dept. E15, D-80747 Garching bei München, Germany

[2] **Max-Planck-Institut für Physik**
Föhringer Ring 6, D-80805 München, Germany

At the Technical University of Munich and the Max Planck Institute of Physics we are developing cryogenic detectors for the detection of small deposited energies, for example from the elastic scattering of WIMPs or neutrinos, or the absorption of X-rays. This preprint contains reports of our work which we have presented at the Fifth International Workshop on Low Temperature Detectors (LTD-5), 29 July - 3 August 1993, Berkeley, California and a review on *"Cryogenic Detectors for Dark Matter Searches"* presented at TEXAS/PASCOS '92. Also available as a preprint is M. Frank's PhD thesis in German: *"Entwicklung eines Niederenergie-Kalorimeters mit supraleitendem Phasenübergangsthermometer,"* MPI-PhE/93-16.

1. Cryogenic Detectors for Dark Matter Searches

Cryogenic Detectors for Dark Matter Searches,
a review by W. Seidel.

Munich Dark Matter Search,
W. Seidel, P. Colling, S. Cooper, D. Dummer, F. v. Feilitzsch, P. Ferger, G. Forster, M. Frank, H.-J. Gebauer, J. Igalson, E. Kellner, U. Nagel, A. Nucciotti, F. Pröbst, A. Rulofs, and L. Stodolsky.

2. Cryogenic Calorimeters

Physics and Performance of Calorimetric Particle Detectors with Dielectric Absorbers and Superconducting Phase Transition Thermometers,
M. Frank, P. Colling, S. Cooper, D. Dummer, F. v. Feilitzsch, P. Ferger, G. Forster, H.-J. Gebauer, J. Igalson, E. Kellner, U. Nagel, A. Nucciotti, F. Pröbst, A. Rulofs, W. Seidel, and L. Stodolsky.

Calorimeters with Proximity-Effect Thermometers and Lead and Tin Absorbers,
G. Forster, K. Hallatschek, D. Wilhelm, F. Pröbst, W. Seidel, E. Kellner, F. v. Feilitzsch.

For our first results with a calorimeter with a tungsten thermometer see paper on tungsten films by P. Colling, et al. under 3.

---

* Present Address: Radiometric Physics Division, NIST, Gaithersburg, MD 20899, USA.

$ Permanent Address: Polish Academy of Sciences, Institute of Physics, Warsaw, Poland.

& Permanent Address: Institute of Chemical Physics and Biophysics, Rävala pst. 10, EE0001 Tallinn, Estonia.

3. Thin Films and Phase Transition Thermometers

Physics, Fabrication and Characterization of Thin Films,
H. Kraus, M. Gutsche, J. Jochum, and B. Kemmather.

Superconducting Tungsten Films for Use as Phase Transition Thermometers for Calorimetric Detectors,
P. Colling, A. Nucciotti, W. Seidel, F. Pröbst, S. Cooper, D. Dummer, P. Ferger, M. Frank, J. Igalson, U. Nagel, A. Rulofs, and L. Stodolsky.

Use of Proximity Effect in Iridium-Gold Superconducting Phase Transition Thermometers,
U. Nagel, A. Nowak, E. Kellner, H.-J. Gebauer, P. Colling, S. Cooper, D. Dummer, P. Ferger, M. Frank, P. Freund, G. Forster, J. Igalson, A. Nucciotti, F. Pröbst, A. Rulofs, W. Seidel, and L. Stodolsky.

4. Superconducting Tunnel Junctions

Signal to Noise Ratio of Superconducting Tunnel Junction Detectors,
J. Jochum, H. Kraus, M. Gutsche, and B. Kemmather.

Photolithographic Fabrication of Tunnel Junction Detectors,
B. Kemmather, H. Kraus, J. Jochum, and M. Gutsche.

Cryogenic Detectors for Dark Matter Searches

W. SEIDEL
Max-Planck-Institut für Physik
Föhriger Ring 6, 8000 München 40
Germany

Introduction

One of the fundamental questions of astrophysics and cosmology is the nature of the dark matter. The observation of the rotational velocity of stars in spiral galaxies enables us to calculate the mean density of matter as a function of distance from the galactic centre. The matter distribution obtained in this way is in strong disagreement with the observed distribution of luminous matter. [1, 2]. This disagreement is attributed to the existence of a halo of invisible ("dark") matter. This halo of dark matter extends well beyond the visible matter and is the dominant contribution (90%) to the total mass of a galaxy. The mean density of dark matter (DM) at the position of our solar system in our galaxy was estimated to be [1]

$$\rho_{DM} = 0.3\, GeV/cm^3.$$

The nature of this dark matter is still unknown. It can consist of baryonic matter as for example gas, dust and faint or non-luminous stars. An alternative is the existence of stable neutral elementary particles with a non-vanishing mass. One group of candidates are WIMPs (weakly interacting massive particles) with the lightest supersymmetric particle as the presently favoured candidate.

Direct Detection of WIMPs

One way to search directly for WIMPs is to consider their elastic scattering on nuclei. This process transfers a recoil energy ΔE to the nucleus.

$$\Delta E = \frac{m_n m_d^2}{(m_n + m_d)^2} v^2 (1 - cos\theta),$$

where m_n is the mass of the nucleus, m_d the mass of the dark matter particle, v the velocity of the dark matter particle, and θ the scattering angle in the center of mass system. In the rest frame our galaxy the velocity of the WIMPs is assumed to be a Maxwell-distribution ($V_{rms} \approx 250 - 300\,\mathrm{km/s}$) with an upper cutoff at the escape velocity of approximately 500 km/s. The velocity distribution we would observe on earth is modified due to the movement of our solar system around the galactic centre with a speed of 220 km/s. For WIMP masses in the GeV range one expects nuclear recoil energies in the keV range. The present experimental limits are given by low radioactive background silicon and germanium ionization detectors [3, 4, 5]. Due to the low ionization efficiency of low energy nuclear recoils the detection threshold of

Presented at the combined 16th Texas Symposium on Relativistic Astrophysics and the 3rd International Symposium on Particles, Strings, and Cosmology (TEXAS/PASCOS '92), 13-18 July 1992, Berkely, California. Published in Annals of the New York Academy of Science, ***668****, pg. 632 (1993).*

the germanium detectors is quite high (15 keV) for nuclear recoils. In the range of lower WIMP masses (in the order of 30 GeV) they are therefore only sensitive to a small fraction of the velocity distribution. Detectors with lower threshold would be helpful in this mass range. It is also desirable to use other detector materials or to have detectors providing a discrimination between events induced by photons and events induced by nuclear recoils. To meet this demands different types of cryogenic detectors are presently under development.

Cryogenic Detectors

In general a detector counts the excitations in a gas, liquid or solid created by the interaction with a particle. In conventional detectors these excitations are ions, electrons, photons, or electron hole pairs, whose energies are on the order of eV. The energy resolution is ultimately limited by the statistical fluctuations in the number of excitations created. To improve the energy resolution one has to count other types of excitations with lower energies, such as phonons in solids or quasiparticles in superconductors. These excitations have energies on the order of meV or lower. To avoid their thermal excitation such a detector has to be at low temperatures.

Low temperature detectors should therefore be able to achieve lower energy thresholds, higher energy resolutions, and to use a wide range of detector materials.

If a particle interacts in a cryogenic detector many excitations are created. Being not in thermal equilibrium these excitations decay and finally reach thermal equilibrium. The duration of this thermalization process is called thermalization time. Most cryogenic detectors can be attributed to two classes:

- Thermal detectors. In this class of detectors one waits until a thermal equilibrium is established and a temperature can be measured. Therefore these devices are slow with typical time scales in the millisecond regime. They usually provide energy-resolution, are relatively "simple" and can be made out of a wide range of materials. All different types of calorimeters and the granule detector belong to this class.

- Nonthermal detectors. This class of detectors measures the excitations during the thermalization process. They provide energy and position-resolution with typical time scales in the microsecond regime. The physics of this class of detectors is more complicated giving stronger restrictions to the detector materials that can be used. Devices using superconducting tunnel junctions or arrays of superconducting tunnel junctions and a detector called SiCAD belong to this class.

A detailed description of the principles and present status of cryogenic detectors can be found in the literature [6]. I will therefore concentrate on devices which are already used or are close to be used in experiments. All these devices are calorimeters.

Calorimeters

A calorimeter consists of an absorber in which the particle interaction takes place and a thermometer attached to the absorber. The basic idea of an calorimeter is to wait until the high energy phonons created by a particle interaction have thermalized,

thermometer and absorber are in thermal equilibrium and the temperature of the calorimeter can be measured. The change in temperature ΔT due to an energy deposition E is given by

$$\Delta T = \frac{E}{C},$$

where C is the heat capacity of absorber plus thermometer. To cool down to its equilibrium temperature after an event the calorimeter is connected to a heat sink via a thermal link with thermal conductance g. The time constant τ for cooling, which is the decay time of a pulse is

$$\tau = \frac{C}{g}.$$

One has to keep the heat capacity C low in order to obtain large signals. To allow high absorber masses the specific heat capacity per unit mass of the absorber material has to be low. For dielectric materials the specific heat capacity is proportional to $(T/\Theta_D)^3$, where T is the temperature and Θ_D is the Debye-temperature of the material used. Since the heat capacity decreases when one lowers the temperature, one can gain a lot in sensitivity if running a calorimeter at the lowest possible temperatures. Furthermore materials with a high Θ_D should be preferred.

The essential part of a calorimeter is the thermometer. I will concentrate on two types of thermometers, doped semiconductors and superconductors.

Calorimeters with Semiconducting Thermometers

At low temperatures doped semiconductors show an increasing electrical resistance for decreasing temperatures due to the freezing out of free charge carriers. They can therefore be used as thermometers. The most widely used semiconducting thermistors are neutron transmutation doped (NTD) germanium thermistors [7, 8]. Calorimeters with semiconducting thermistors can be operated over a wide temperature range. Since semiconducting thermistors have a high impedance they are well matched to conventional electronics. To avoid long RC time constants due to stray capacitances, the leads to the thermistors have to be short. This problem is usually solved by using preamplifiers with cold input stages. One also has to take care to suppress noise due to microphonics.

Building a calorimeter the semiconducting thermistor is simply glued to the absorber. Groups developing this type of detector claim that these devices can be described by a purely thermal model.

In France a group has built a detector consisting of a 24 g sapphire absorber with a 1.28 mm^3 NTD germanium thermistor [9, 10]. The device was operated at 55 mK. This detector showed a resolution of 3.7 keV (FWHM) for 60 keV photons. With this detector first background tests in the Fréjus tunnel were performed. For doing a dark matter search a new low radioactive background cryostat has been built and will soon be installed underground.

An Italian group is already running an experiment with a low temperature calorimeter searching for the $0\nu\beta\beta$-decay of ^{130}Te [11, 12]. They constructed a calorimeter with a 73.1 g single crystal of telluriumoxide as absorber and a NTD germanium thermistor. The operating temperature is 16 mK. They use a specially built low radioactive background dilution refrigerator surrounded by an outer lead shield. To minimize RF interference the cryostat is placed in a Faraday cage. The whole

experiment is located in the Gran Sasso Underground Laboratory. The calorimeter shows an energy resolution between 5 and 10 keV at energies ranging from 300 keV to 6 MeV. After an accumulated running time of 1389 hours they have seen no evidence for the $0\nu\beta\beta$-decay of ^{130}Te. Their lower limit for the lifetime in the 0ν-channel $\tau_{0\nu}$ is $\tau_{0\nu} > 2.5 \times 10^{21}$ years (90%*c.l.*). This result is three orders of magnitude more stringent than results for the same nucleus obtained with conventional detectors. With an improved shielding they recently lowered their radioactive background by one order of magnitude. They are preparing an experiment with four telluriumoxide crystals of a mass of 350 g each. They also have enriched ^{130}Te and plan to build a calorimeter out of this material. Furthermore they recently published some new ideas for the detection of solar neutrinos with cryogenic detectors [13].

Very interesting is the simultaneous measurement of phonons and ionization. By building a device which acts as an ionization detector and as a calorimeter at the same time one can distinguish between nuclear recoil and photon events. Since the ionization efficiency of nuclear recoils is much smaller than that of photo- or Compton-electrons, the fraction of the energy contained in the ionization signal normalized to the total energy deposited (which is measured by the calorimeter) can be used to distinguish nuclear recoil and photon events. Such a device was developed by a group in Berkeley [14, 15]. With a 60 g germanium absorber they obtained an energy resolution of 1.8 keV (FWHM) for the ionization and the thermal signal. They clearly showed the discrimination of recoil and photon events. Since dark matter produces only nuclear recoils this technique can be used to reduce the radioactive background significantly. The energy threshold however will be similar to that of conventional germanium detectors. The Berkeley group is preparing a dark matter experiment which should start to run in 1993.

Calorimeters with Superconducting Thermometers

A superconductor shows a strong temperature dependence of its electrical resistance in a narrow region around its transition temperature T_C. In this transition region the resistance goes from the normal conducting value to zero in the superconducting state. If the whole calorimeter is stabilized right in the transition a temperature rise can be measured as a change in resistance. The particle-induced temperature rise of the thermometer is usually much smaller than the width of the transition.

This type of thermometer is naturally a low impedance device and well matched to a SQUID as preamplifier [16]. The operating temperature of the calorimeter is restricted to the transition region around T_C. First results showed the high sensitivity of this thermometer at high operating temperatures (120 mK). This type of calorimeters are developed by two collaborating groups at the Technical University in Munich and the Max-Planck-Institute for Physics in Munich, Germany. Lower operating temperatures are one of the goals of their work. They try to do this in two ways:

- One can produce thermometers of pure metals with low critical temperature such as tungsten (T_C =15 mK). They succeeded very recently in producing a tungsten film showing a transition at 14 mK [17].

- When a superconducting film is overlaid with a normal conducting film, both act together as a single superconductor with a reduced T_C. This is called the

proximity effect. In principle the critical temperature can be tuned by varying the thicknesses of the normal and the superconducting layer.

In the first attempt to build a calorimeter with an iridium/gold proximity thermometer on a silicon crystal the production process was not yet under control. As a result the thermometer showed a very broad transition, starting at 110 mK and still being not totally superconducting at 20 mK [18]. Due to its flat slope such a thermometer is quite insensitive, but one has the chance to study the behaviour of the calorimeter over a wide temperature range. The absorber used for this calorimeter was a 19 g Silicon crystal. In spite of the insensitive thermometer this calorimeter showed an energy resolution of 1 keV (FWHM) for 60 keV photons. This resolution was achieved at an operating temperature of 20 mK. The shape of the pulses could be fitted with three exponentials, one describing the rise time and two the decay of the pulse. The presence of two decay times and the observed pulse heights are in disagreement with the simple thermal model of a calorimeter. Comparison of pulses taken at different operating temperatures led to the conclusion that the fast part of the pulse is caused by nonthermal phonons and the slow part by thermal phonons. This device is thus a combination of a nonthermal and a thermal detector [19]. Future experiments will show if some position information or information on the nonthermal phononspectrum and type of event (nuclear recoil or photon) can be obtained from the pulse shape.

The results obtained with this quite insensitive iridium/gold thermometer showed the importance of running this type of calorimeter at low temperatures. Meanwhile the production of iridium/gold thermometers on sapphire seems to be under control and different thermometers with narrow transitions (less than 1 mK wide) and critical temperatures down to 38 mK were produced. The planing of a low background set up for a dark matter experiment was just started.

Conclusions

At the present status of development of large mass, low temperature detectors, energy resolutions up to 1 keV and masses up to several hundred grams can be achieved. Such detectors are in some applications already superior to conventional detectors. Futhermore they can be built out of a wide range of materials, providing a higher flexibility in the design of new experiments. Some of them are able to discriminate between events induced by nuclear recoils and events induced by photons giving an additional suppression of the photon background. The relatively slow pulses of low temperature detectors are no limitation when rare processes are to be investigated, as in underground physics.

Several experiments searching for dark matter with cryogenic detectors are in preparation and should give new results in the next years.

References

[1] J. A. R. Caldwell, J. P. Ostriker, Astrophys. J. 251, (1981) 61

[2] V. C. Rubin, Sci. Am. 248, (1983) 88

[3] D. Caldwell, Mod. Phys. Lett. A5 (1990) 203

[4] D. Reusser et al., Phys. Lett. B 255, (1991) 143

[5] D. Caldwell et al., Phys. Rev. Lett. 65 (1990) 1305

[6] Low Temperature Detectors for Neutrinos and Dark Matter IV edited by N. E. Booth and G. L. Salmon Editions Frontières (1991)

[7] Ning Wang, F. C. Wellstood, B. Sadoulet, E. E. Haller, J. Beeman, Phys. Rev. B 41 (1990), 3761

[8] T. W. Kenny, P. L. Richards, I. S. Park, E. E. Haller, J. W. Beeman, Phys. Rev. B 39, 8467

[9] P. de Marcillac, N. Coron, J. Leblanc, C. Goldbach, G. Nollez, A. Vidal-Madjar, J.-P. Torre, J. Mangin, H. Stroke, J. W. Zhou, A. de Bellefon, Y. Giraud-Héraud, L. Gonzales-Mestres, I. Berkèrs, B. Chambon, D. Drain, F. Amoudry, J. Bouchard, N. Coursol, D. Massé, J.-L. Picolo Low Temperature Detectors for Neutrinos and Dark Matter IV Editions Frontières (1991), 81

[10] N. Coursol, N. Coron, D. Massé, H. Stroke, J. W. Zhou, P. de Marcillac, J. Leblanc, G. Artzner, G. Dambier, J. Bouchard, G. Jegoudez, J. P. Lepeltier, G. Nollez, C. Goldbach, J.-L. Picolo, Nucl. Instr. Meth. A312 (1992), 24

[11] A. Alessandrello, C. Bofferio, D. V. Camin, O. Cremonesi, E. Fiorini, G. Gervasio, A. Giuliani, M Pavan, G. Pessina, E. Previtali, L. Zanotti, Phys. Lett. B 285 (1992), 176

[12] A. Alessandrello, C. Bofferio, D. V. Camin, O. Cremonesi, E. Fiorini, G. Gervasio, A. Giuliani, A. Nucciotti, M. Pavan, G. Pessina, E. Previtali, L. Zanotti,Proceedings of "Neutrino 92" Granada (1992)

[13] A. Alessandrello, E. Bellotti, C.Broferio, D.V. Camin, C. Cattadori, O. Cremonesi, E. Fiorini, A. Giuliani, M. Pavan, G. Pessina, E. Previtali, L. Zanotti, preprint INFN/AE-92/25, (1992)

[14] T. Shutt, N. Wang, B. Ellman, Y. Giraud-Heraud, C. Stubbs, P. D. Barnes Jr., A. Cummings, A. Da Silva, J. Emes, E. E. Haller, A. E. Lange, J. Rich, R. R. Ross, B. Sadoulet, G. Smith, W. Stockwell, S. White, B. A. Young, D. Yvon, Phys. Rev. Lett. 69 24 (1992) 3531

[15] T. Shutt, B. Ellman, P. D. Barnes Jr., A. Cummings, A. Da Silva, J. Emes, Y. Giraud-Heraud, E. E. Haller, A. E. Lange, J. Rich, R. R. Ross, B. Sadoulet, G. Smith, W. Stockwell, C. Stubbs, N. Wang, S. White, B. A. Young, D. Yvon, Phys. Rev. Lett. 69 24 (1992) 3525

[16] W. Seidel, G. Forster, W. Christen, F. Feilitzsch, H. Göbel, F. Pröbst and R. L. Mößbauer, Physics Letters B 236 (1990) 483.

[17] W. Seidel, "Superconducting Thin Film Thermometers for Calorimeteric Particle Detectors", to be published in Proceedings of the Twelfth International Vacuum Congress, Vol.3, The Hague, Netherlands, October 1992
and Max-Planck-Institut für Physik, München preprint MPI-PhE/92-24 (1992)

[18] F. Pröbst, S. Cooper, D. Dummer, M. Frank, W.Seidel, Low Temperature Detectors for Neutrinos and Dark Matter IV Editions Frontières (1991), 193

[19] F. Pröbst,"Phonon Mediated Detection of Particles", to be published in Proceedings of the Seventh International Conference on Phonon Scattering in Condensed Matter Ithaca, New York, August 1992
and Max-Planck-Institut für Physik, München preprint MPI-PhE/92-24 (1992)

Munich Dark Matter Search

W. Seidel, P. Colling, S. Cooper, D. Dummer, F.v.Feilitzsch,*
P. Ferger, G. Forster,* M. Frank, H.-J. Gebauer, J. Igalson, E. Kellner,*
U. Nagel, A. Nucciotti, F. Pröbst, A. Rulofs, and L. Stodolsky

Max-Planck-Institut für Physik, Föhringer Ring 6, D-80805 München, Germany
** Technische Universität München, D-85747 Garching, Germany*

We plan a dark matter search using cryogenic calorimetric detectors with superconducting phase transition thermometers. We discuss such an experiment, compare its estimated sensitivity range with other dark matter searches, and discuss its planned realization.

1. INTRODUCTION

We have been developing massive cryogenic calorimeters with very good energy resolution and low energy threshold. The special feature of our work is that we develop our own thermometer, a superconducting phase transition thermometer, with the goal of having significantly better resolution than other groups. We have already achieved promising results,[1–4] such as an energy resolution of 220 eV (FWHM) for 6 keV X-rays with a 31 g sapphire detector, and further progress is expected. We feel it is time to start with an experiment using our detector. We have looked into various uses of our type of detector and agree that a dark matter search is the best choice as a first experiment. In the first stage we want to run a 1 kg sapphire experiment with a threshold of 500 eV in a low background environment. Later we will use larger masses and other target materials.

The following sections compare a dark matter search with our detector with the planned dark matter searches of other groups and give a description of the experimental requirements.

2. SEARCHING FOR WIMP DARK MATTER

Weakly interacting massive particles (WIMPs) are candidates for dark matter. The lightest supersymmetric particle is presently the theoretically favoured candidate. Accelerator experiments such as ALEPH and CDF can give limits on the allowed mass range for the lightest supersymmetric particle, restricting its mass to be larger than 20 GeV. However this is only valid within certain parameter regions of the minimal supersymmetric model, which has itself not yet been experimentally

Presented at the Fifth International Workshop on Low Temperature Detectors (LTD-5), 29 July – 3 August 1993, Berkeley, California. To be published in Journal of Low Temperature Physics.

confirmed. Therefore we feel that it is important to search the mass and cross section regions as widely as experimentally feasible, independent of models.

The way to search directly for WIMPs is to look for their elastic scattering on nuclei. This process transfers a recoil energy ΔE to the nucleus:

$$\Delta E = \frac{m_n m_d^2}{(m_n + m_d)^2} v^2 (1 - cos\theta), \tag{1}$$

where m_n is the mass of the nucleus, m_d the mass of the dark matter particle, v the velocity of the dark matter particle, and θ the scattering angle in the center of mass system. In the rest frame of our galaxy the velocity of the WIMPs is assumed to be a Maxwell distribution ($V_{rms} \approx 300\,\mathrm{km/s}$) with an upper cutoff at the escape velocity of approximately 500 km/s. The velocity distribution we would observe on earth is modified due to the movement of our solar system around the galactic centre with a speed of 220 km/s. Folding this velocity distribution with the distribution of ΔE results in a nuclear recoil energy spectrum that falls off roughly exponentially. The characteristic energy of the spectrum depends on both the WIMP mass and the target nucleus mass. Due to the movement of the earth around the sun, the speed of the earth around the galactic center has an additional annual modulation of about 10%, resulting in a roughly 10% annual modulation of the shape of the recoil spectrum. The number density of WIMPs is assumed to be that needed to explain the rotation curve of our galaxy: about 0.3 GeV/cm^3 in our region. Thus the detection rate for WIMPs in a detector depends on the WIMP's mass, its interaction cross section with the chosen target nucleus, and the experimental threshold.

For WIMP masses in the GeV range one expects nuclear recoil energies in the keV range. To be sensitive to a spin-dependent interaction of WIMPs, as for photinos, one needs detectors made of nuclei with a net spin. The lower range of WIMP masses an experiment can cover is mainly determined by the energy threshold of the detector. To be sensitive to low interaction cross sections one needs a large detector mass (to increase the total rate) as well as very low radioactive background in the energy region of interest. The latter has become a field of research of its own, pioneered by the experiments searching for $\beta\beta$-decay.

3. COMPARISON OF DARK MATTER SEARCH EXPERIMENTS

The present experimental limits for WIMP dark matter are given by low background silicon and germanium ionization detectors.[5–7]

Among experiments planned by other groups are those using liquid or solid scintillators and a cryogenic germanium calorimeter which simultaneously measures ionization. In the following section we compare the sensitivity range of these experiments. To do this one has to take into account the properties of the different detectors.

- NaI scintillator.[8]
  A 1 kg prototype of a NaI scintillator has an energy threshold of 4 keV for γ's, which due to the poorer ionization efficiency for slow recoil nuclei corresponds to 16 keV for Na nuclear recoils and 60 keV for I recoils. The energy resolution

is 12.5 keV (FWHM) for 88 keV photons. A total detector mass of 100 kg is planned.

- Liquid Xenon scintillator.[9]
  The liquid Xenon scintillator has presently an energy threshold of roughly 12 keV for electrons corresponding to a energy threshold of 60 keV for nuclear recoils. Its energy resolution is 57 keV (FWHM) for 88 keV photons. At present masses up to 2 kg can be realized.

- The combination of a cryogenic calorimeter with an ionization detector.[10]
  Discrimination between nuclear recoils and electron or photon induced events in the detector, may allow the radioactive background to be reduced by two orders of magnitude. The threshold is about 12.5 keV for nuclear recoils and the energy resolution about 1.8 keV (FWHM) for 60 keV photons. Masses of about 1 kg seem feasible. The only stable isotope of germanium with nuclear spin (^{73}Ge) has a natural abundance of 7.8%. The USCB/LBL/UCB group has enough enriched ^{73}Ge for a 0.5 kg detector.

- Our cryogenic calorimeters will have low thresholds of about 500 eV for nuclear recoils and have now an excellent energy resolution of 220 eV (FWHM) for 6 keV photons.[1] We plan to use 1kg of sapphire for an initial experiment. In contrast to the other detectors a wide range of absorber materials can be used.

These detector properties influence the sensitivity range and the signatures for dark matter that can be used by different experiments.

In Fig. 1 we show a rough estimate of the upper limits which different proposed detectors could set on dark matter particles. It assumes a measuring time of 1 year and a flat background of 1 count/kg/keV/day. The calculations were made for a detector made of 0.5 kg enriched ^{73}Ge (threshold 12.5 keV) with a background suppression of 99%, 100 kg NaI scintillator (threshold 16 keV), and 1 kg sapphire calorimeter (threshold 0.5 keV). The energy resolution and ionization efficiency for the different detectors are taken into account. For WIMP masses below 20 GeV a detector with a low threshold as ours is needed. For large WIMP masses all detectors are about equal, because most of the recoil spectrum is above all the thresholds, and the sensitivity is then given mainly by the detector mass, the measuring time, and the background rate.

The WIMP cross section depends however on the detector nucleus (due to a kinetic and, for spin dependent interaction, a spin factor). To compare different experiments the curves in fig. 1a have been converted into cross sections for WIMP proton scattering $\sigma_{(W-p)}$ (fig. 1b) assuming spin dependent interaction. This was accomplished by applying equation 2 to all sensitivity limits.

$$\sigma_{(W-p)} = \sigma_{(W-N)} \frac{\mu^2_{(W-p)} \lambda^2_p J_p(J_p+1)}{\mu^2_{(W-N)} \lambda^2_N J_N(J_N+1)}, \qquad (2)$$

where $\sigma_{(W-N)}$ is the cross section for a WIMP scattering at a nucleus, μ_{W-p} and μ_{W-N} are the reduced masses of the WIMP-proton and the WIMP-nucleus system, and ($\lambda^2_p J_p(J_p+1)$ and $\lambda^2_N J_N(J_N+1)$) are the nuclear spin factors.[11] If the valence

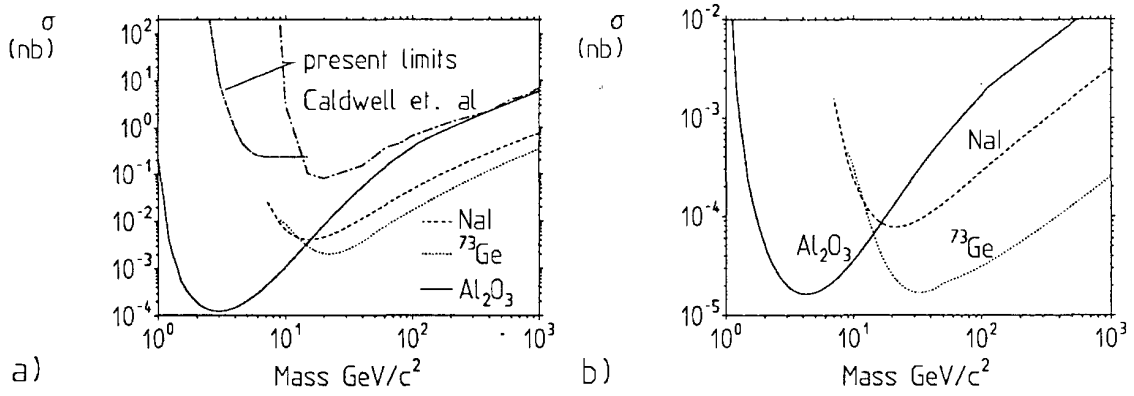

Fig. 1: a) Rough estimate of sensitivities of different experiments assuming a background of 1 count/(keV kg day). The sensitivities of a 100 kg NaI, a 0.5 kg ^{73}Ge with 99% background rejection, and 1kg sapphire detector are shown. b) Sensitivities of the NaI, ^{73}Ge, and Al_2O_3 detector referred to the cross section of a WIMP scattering on a proton assuming spin dependent interaction.

nucleon of the target nucleus is a neutron, equation (2) has additionally to be multiplied by a factor C_p/C_n, where C_p and C_n are the squared expectation values of the hadronic matrix elements for photino elastic scattering off a proton or neutron respectively.[11]

As it can be seen in fig. 1 the sapphire calorimetric detector is superior in the low mass range.

A positive signature for dark matter signals could be given by the observation of an annual modulation of the recoil spectrum. This is a 10 % effect and its detection requires very good statistics and therefore high detector masses such as the NaI scintillator.

A stronger effect for low WIMP masses is the variation of the recoil spectrum with the mass of the target nucleus. To use this effect one has to be able to build the detector out of different materials. Moderate energy resolution is necessary to see the shape of the recoil spectrum. Understanding the shape of the radioactive background is also very important, and this requires a good energy resolution for example for the identification of X-ray lines. An example of the variation of the recoil spectrum (without background) for 5 GeV WIMPs is shown in Fig. 2 for absorbers which we may use.

4. EXPERIMENTAL SET-UP

For an experiment it is of extreme importance to reach the lowest possible radioactive background. This requires a major effort and attainment of experience beyond our detector development work. To avoid background events induced by cosmic rays the whole experiment will be located in an underground laboratory such as the Gran Sasso Laboratory, where we have requested space. In addition it will be carefully shielded against the natural radioactivity of the surrounding rocks. All materials in the shielding and the vicinity of the detector will be specially

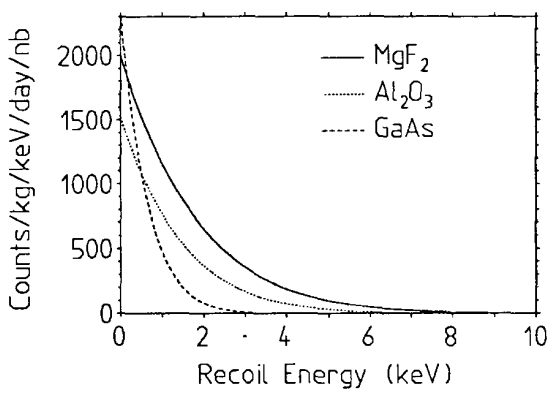

Fig. 2: Expected recoil spectrum for a 5 GeV WIMP on various absorbers that we may use: MgF_2, Al_2O_3, and GaAs.

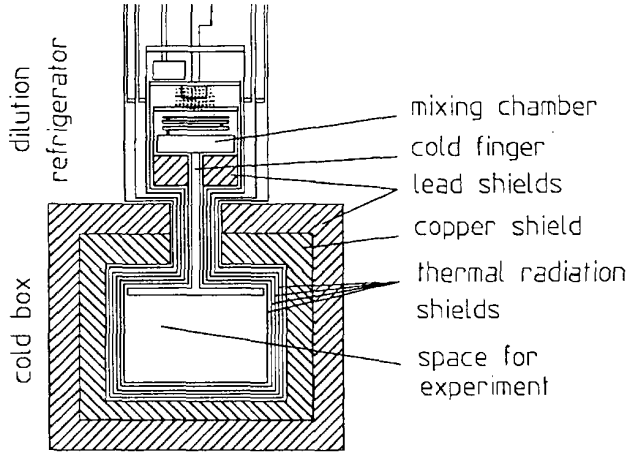

Fig. 3: Sketch of layout of dilution refrigerator and cold box.

selected for their radioactive purity. Because not all materials necessary for building a dilution refrigerator are radiopure it is necessary to divide the experimental set-up in two parts: one containing the dilution refrigerator and the other one containing the calorimeter surrounded by very low background materials and shielding. The cooling power of the refrigerator is transferred into this cold box by a cold finger protected by thermal radiation shields. The space for experiments in this cold box will be about 30 liters. To hang this cold box right under the dilution refrigerator is the simplest solution from the mechanical and cryogenic point of view (Fig. 3). The line of sight into this shielding will be blocked by an additional shield. For first cryostat and calorimeter tests we will make a smaller, simpler cold box.

The experiment will be shielded from electromagnetic interference by a Faraday cage and from the earth's field by a magnetic shielding. In addition it will be vibrationally isolated from the pumps of the gas handling system.

We have begun to develop radiopure cold seals to replace the usual indium

seals. We are also checking sapphire crystals of different suppliers using different crystal growth methods for their radioactive contaminations by neutron activation analysis. First results show that crystals can be obtained with uranium, thorium, and potassium contaminations below our present detection limits (see table 1). The

element	det. limit [ng/g]
U	< 0.019
Th	< 0.002
K	< 1764

Table 1: table of our present neutron activation detection limits for different elements in sapphire.

detection limit of potassium corresponds to an detection limit of 0.21 ng/g for ^{40}K. The high detection limit for K results from the high activation of the sapphire matrix. We will therefore look for other methods to obtain a better limit on a possible ^{40}K contamination.

We are also performing Monte Carlo simulations to understand the effect of the internal contaminations of the detector and will soon start a simulation of our cold box shielding.

5. CONCLUSIONS

We are planning a WIMP dark matter search using our cryogenic calorimetric detectors. We expect our experiment to be superior in the low WIMP mass range to other experiments being planned and therefore to be complementary to other dark matter searches. Due to the possibility of varying the target nucleus cryogenic calorimetric detectors also allow a positive confirmation of dark matter particles within their sensitivity range.

REFERENCES

1. M. Frank et al. these proceedings.
2. U. Nagel et al. these proceedings
3. P. Colling et al. these proceedings
4. G. Forster et al. these proceedings
5. D.O. Caldwell et al., Phys. Rev. Lett. 61, 510 (1988)
6. D. Reusser et al., Phys. Lett. B 255, 143 (1991)
7. D.O. Caldwell et al., Phys. Rev. Lett. 65, 1305 (1990)
8. C. Bacci et al. (BRS coll.), Phys. Lett. B 293, 460 (1992)
9. Belli et al. (DAMA coll.), Gran Sasso preprint LNGS 93/55 (1993)
10. D.O. Caldwell in Low Temperature Detectors for Neutrinos and Dark Matter IV, Oxford 1991, Editions Frontieres, p.387; see also P. Barnes et al., these proceedings.
11. J. Ellis, R.A. Flores, Nucl. Phys. B 307, 883 (1988)

Physics and Performance of Calorimetric Particle Detectors with Dielectric Absorbers and Superconducting Phase Transition Thermometers

M. Frank, P. Colling, S. Cooper, D. Dummer, F. v. Feilitzsch,*
P. Ferger, G. Forster,* H.-J. Gebauer, J. Igalson, E. Kellner,* U. Nagel
A. Nucciotti, F. Pröbst, A. Rulofs, W. Seidel, L. Stodolsky

Max-Planck-Institut für Physik, Föhringer Ring 6, D-80805 München, Germany
**Technische Universität München, D-85747 Garching, Germany*

We present results obtained with detectors consisting of dielectric absorber crystals and superconducting phase transition thermometers made of Ir/Au bilayers. With a 31 g sapphire crystal and an Ir/Au thermometer operated at 45 mK we have obtained an energy resolution of 220 eV (FWHM) for collimated 5.9 keV X-rays. To explain the measured pulse shapes we have developed a model which includes the effect of non-thermal phonons. Results obtained previously with a 18 g Si absorber and an Ir/Au thermometer with broad transition allowed checking this model over a wide temperature range. A heater experiment performed with this calorimeter provides further support of our model.

1. INTRODUCTION

We are developing massive cryogenic calorimeters which consist of a dielectric absorber crystal and a small thin film of superconducting material evaporated onto the surface of the absorber crystal serving as a superconducting phase transition (SPT) thermometer. The calorimeter is operated within the transition between the superconducting and the normal conducting state of the film, where the electrical resistance of the film shows a strong dependence on the temperature. A tiny rise in the film temperature resulting from a particle interaction in the absorber can cause a measurable rise in the film's resistance. For a small temperature rise the film remains well within its transition and the detector response is linear. A weak thermal link allows the calorimeter to cool back to the equilibrium temperature after an interaction.

Here we describe results obtained with calorimeters utilizing iridium/gold bilayers as SPT thermometers. In these Ir/Au bilayers the critical temperature of the Ir is depressed below its bulk T_c value of 112 mK by the presence of the normal conducting Au by means of the proximity effect. The critical temperature of

Presented at the Fifth International Workshop on Low Temperature Detectors (LTD-5), 29 July - 3 August 1993, Berkeley, California. To be published in Journal of Low Temperature Physics.

a bilayer is tunable by a proper choice of the film thicknesses.[1] Our latest results obtained with W thermometers with a T_c close to the bulk W value of 15 mK are presented elsewhere in these proceedings.[2] Results with pure Ir thermometers have been reported previously.[3,4]

2. EXPERIMENTS

In the following we describe results obtained with two calorimeters, one with a sapphire absorber and one with a silicon absorber. In each case the crystal dimensions were 4 cm × 2 cm × 1 cm and the thermometer consisted of a 2.5 mm × 1 mm Ir film covered by a 2.5 mm × 1.5 mm Au film. The resistance of the film (~0.1 Ω) is measured by passing a constant current through a circuit in which the film is in parallel with a 0.05 Ω resistor and the pickup coil of a SQUID. A particle-induced rise in the film resistance is measured via the current rise through the SQUID. Experimental details have been published elsewhere.[4]

2.1. 31 g Sapphire Calorimeter operated at 45 mK

The thermometer of this calorimeter consisted of Ir and Au films of thickness 135 nm and 100 nm, respectively. It had a critical temperature of about 45 mK and a transition width of less than 0.5 mK. To reduce the event rate caused by the natural radioactive background in the laboratory the calorimeter was surrounded by a lead shield of wall thickness 2-3 cm suspended from the mixing chamber of our cryostat. A 1 mm diameter spot on the absorber crystal was irradiated through a collimator by X-rays from an ^{55}Fe source, which was mounted inside the shield. Fig. 1a shows a pulse height spectrum. The two Mn X-rays lines (5.89 and 6.49 keV) emitted by the source are well resolved. The resolution of the dominant 5.89 keV line is 220 eV (FWHM). The trigger threshold at about 1.5 keV is set by electronics. Due to pile-up we can only give an upper limit for the baseline noise of 170 eV.

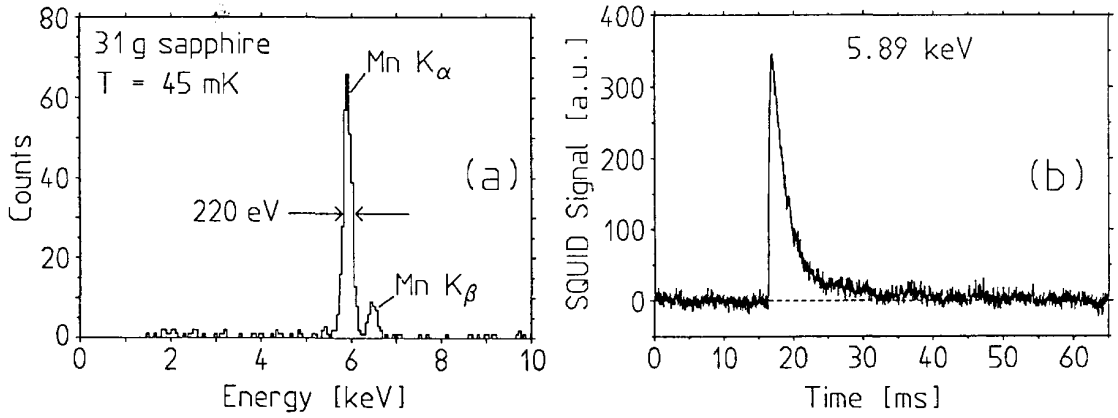

Fig. 1: **Sapphire Calorimeter: (a)** Pulse height spectrum obtained irradiating the calorimeter with 5.89 and 6.49 keV Mn X-rays. The resolution of the 5.89 keV line is 220 eV (FWHM). **(b)** Single 5.89 keV event measured with a bandwidth from DC to 25 kHz.

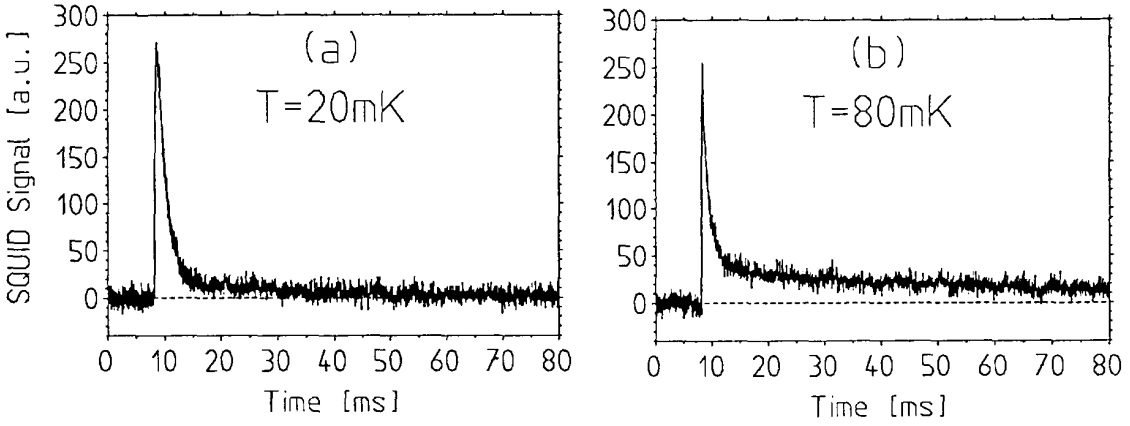

Fig. 2: **Silicon Calorimeter:** **(a)** Single 60 keV pulse recorded at 20 mK; **(b)** ~500 keV background pulse recorded at 80 mK. The comparison shows the significant change in the pulse shape with operating temperature.

Fig. 1b shows a single 5.89 keV event exhibiting two pulse components – a pronounced fast one with a decay time of ~2 ms and a small slow one with a decay time of about 13 ms. The origin of these components is explained below.

2.2. 18.3 g Silicon Calorimeter operated between 17 mK and 112 mK

The thermometer of this calorimeter consisted of Ir and Au films of thickness 40 nm each. In this first attempt to use a Ir-Au proximity thermometer the fabrication process was not yet under control, resulting in a very broad transition curve ranging from 112 mK to below 17 mK. Preliminary results with this calorimeter were already presented at LTD-4 in Oxford.[4] Here we present results of a systematic study of the detector response, which due to the broad transition could be performed in a wide temperature range.[5] In these measurements the whole calorimeter was irradiated with 60 keV photons from an ^{241}Am source placed outside the cryostat.

One striking result of this study was the change of pulse shape with operating temperature. Fig. 2a shows a single 60 keV pulse recorded at 20 mK, Fig. 2b shows a pulse from a higher energy background photon recorded at 80 mK. The pulses have two exponential components: a fast one with a decay time of ~1.5 ms at all operating temperatures, and a slow one with a temperature-dependent decay time varying from 30 to 80 ms. At the higher operating temperatures (~80 mK) the amplitude of the slow component is approximately as expected from the heat capacity of the absorber and the deposited energy. However, at lower temperatures it becomes smaller than expected from the heat capacity, with two orders of magnitude missing at 20 mK (Fig. 4a). The amplitude of the fast component and hence the energy resolution increases with decreasing operating temperatures (Fig. 4b).

In the following section a model of the detector will be presented, which explains the time structure of the pulses and the suppression of the thermal component at low temperatures.

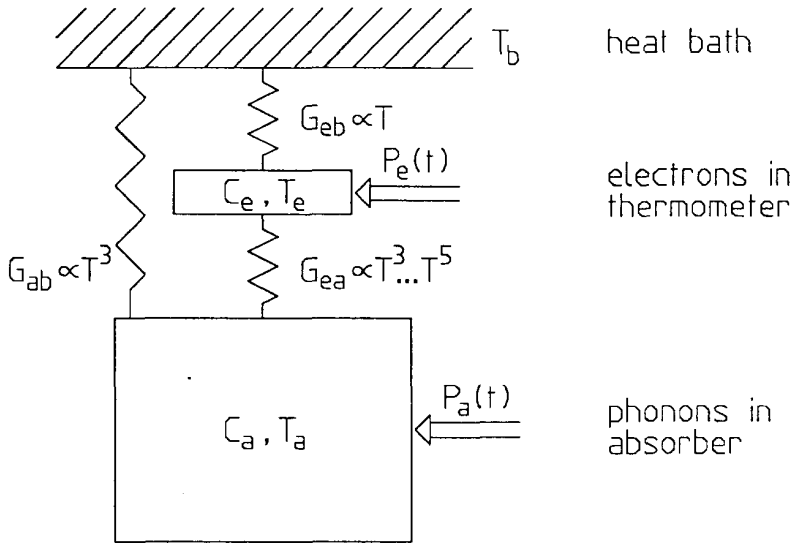

Fig. 3: Our model for cryogenic calorimeters with dielectric absorbers and SPT thermometers.

3. THE MODEL

Fig. 3 shows a model of our detector. Here we describe only qualitatively the main features of this model and how the pulse formation can be understood in terms of this model. A complete, quantitative presentation is given elsewhere.[5]

In this model, the electrons and phonons of the thermometer film are considered as subsystems weakly coupled by $G_{ep} \propto T^5$. The phonons in the film and in the absorber are coupled by the Kapitza conductance $G_K \propto T^3$ across the interface. This results in a total thermal coupling G_{ea} between electrons in the thermometer and phonons in the absorber of $G_{ea}^{-1} = G_{ep}^{-1} + G_K^{-1}$. G_{eb} is the direct coupling of the electrons to the thermal bath, which is provided by a gold wire with thermal conductance $G_{Au} \propto T$, ultrasonically bonded between one side of the thermometer and the sample holder, which acts as the heat bath. $G_{ab} \propto T^3$ accounts for a direct coupling of the absorber phonons to the bath due to its mechanical mounting on ruby spheres.

A two-component pulse of the electron temperature (which is the measured quantity) is formed in the following way. A particle interaction in the absorber creates highly non-thermal phonons, which after a few surface reflections fill the absorber homogeneously within ~10 μs. This time is short compared to our signal rise time (several 10 - 100 μs). Even on ms time scales these phonons do not thermalize in the bulk of our dielectric crystals – the anharmonic phonon decay[6] in Si degrades the phonons rapidly only down to an average frequency of $\nu \sim 0.3$ THz, which is the frequency of the dominant phonons of a 5 K Planck distribution. However, the high-frequency phonons are efficiently absorbed by electrons in the thermometer, which acts as a collector for these phonons. Due to the strong interaction among the electrons, the energy of a phonon transferred to a single electron is quickly thermalized within the electronic subsystem. Thus the flux of high-frequency phonons corresponds to a power input $P_e(t)$ into the electron system, which can heat the

electrons to above the absorber temperature and give rise to the fast pulse component. The energy density of the high frequency phonon population in the absorber and thus $P_e(t)$ are exponentially decreasing. For the calorimeters described here, the "dying-out time" of the high-frequency phonons appears as the fast pulse decay time.

The slow part of the pulse is the temperature rise of the absorber as seen by the electrons of the thermometer. The absorber is heated in two ways: firstly, by the fraction of absorbed high-frequency phonon energy flowing back into the absorber from the thermometer film and, secondly, by a possible thermalization of high frequency phonons on the crystal surface.[7] The power input $P_a(t)$ into the absorber accounts for the latter.

Compared to the absorber temperature rise ΔT_{Debye} expected from its Debye heat capacity and the energy deposition, the amplitude of the thermal part of the pulse is suppressed at low temperatures. This can be explained by the very weak coupling between electrons and thermal phonons, which can become even smaller than G_{eb} at these temperatures. This has two consequences:

- Part of the energy thermalized by the conduction electrons in the film is not re-emitted back into the absorber via G_{ea}, but escapes via G_{eb} into the heat bath and consequently does not heat up the absorber.

- The thermometer "sees" only a fraction of the actual temperature rise of the absorber. Analogous to a resistive voltage divider $G_{eb} \gg G_{ea}$ keeps the electron temperature much closer to the bath temperature than to the absorber temperature.

The model was confirmed in a heater experiment performed with the Si calorimeter. A metal film heater sputtered onto the absorber was used to create thermal phonons. The thermometer signals after a short current pulse through the heater film showed only a slow thermal component – consistent with its amplitude and decay time with the thermal component of particle-induced events of the same energy. The absence of a fast component in the heater pulses confirms the non-thermal origin of the fast component of particle-induced events.

Fig. 4 shows the measured amplitudes of the thermal (a) and the non-thermal (b) component of 60 keV pulses as a function of the operating temperature together with a *simultaneous* fit of the model to these data. The model describes the temperature behaviour of the amplitude of the thermal component very well. At low temperatures the amplitude of the non-thermal component is reproduced by the fit within twice the experimental errors, at high temperatures to at least within a factor two. The discrepancy at the higher temperatures is probably due to a deviation of the T^5 law for G_{ep}, which is expected to affect A_{th} less. Considering the large change of G_{ea} in the shown temperature range the agreement between model and data seems rather good even for the non-thermal component.

4. CONCLUSIONS

With a 31 g sapphire calorimeter with an Ir/Au proximity thermometer we have achieved an energy resolution of 220 eV for 5.89 keV X-rays. This result was

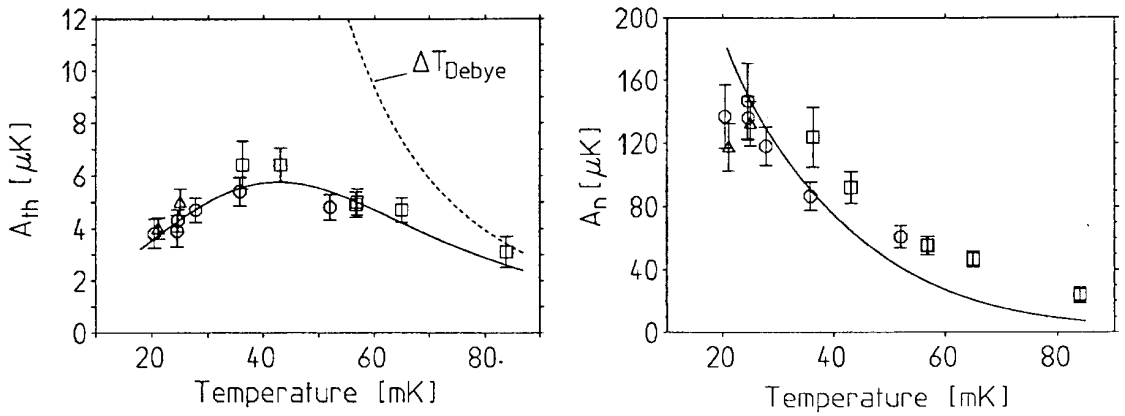

Fig. 4: **Silicon Calorimeter: (a)** Measured amplitude A_{th} of the thermal component of 60 keV pulses as function of operating temperature. The solid line is a fit of the model. The dashed line is the hypothetical temperature rise calculated from the energy deposition and the Debye heat capacity of the absorber. **(b)** Measured amplitude A_n of the non-thermal component of 60 keV pulses; the solid line is a fit (simultaneous with A_{th}) to the model.

rendered feasible by our progress in producing Ir/Au thermometers with low T_c and steep transition. It seems very promising for a dark matter experiment.[8]

The experimental pulses consist of a fast non-thermal and a slow thermal part. A heater experiment confirmed the non-thermal origin of the fast pulse component. We developed a model to explain our experimental pulse shape. We investigated the changes of the pulse shape with operating temperature using an 18 g Silicon calorimeter with an Ir/Au thermometer with broad transition. These data and the data from the 31 g Sapphire calorimeter are in rather good agreement with the model. This model will help in further design and optimisation of our detectors.

ACKNOWLEDGMENTS

We thank A. Singsaas for designing and setting-up the dilution refrigerator used for the experiments, K. Neumaier for providing thermometers and the Crystal Laboratory of the TU München for cutting and polishing the absorber crystals.

REFERENCES

1. U. Nagel, et al., these proceedings.
2. P. Colling, et al., these proceedings.
3. W. Seidel, et al., Phys. Lett. B 236, 483 (1990).
4. F. Pröbst,et al., in *"Low Temperature Particle Detectors for Neutrinos and Dark Matter IV,"* Oxford 1991, Editions Frontieres, p. 193.
5. M. Frank, PhD thesis (in German), June 1993; MPI preprint MPI-PhE/93-16.
6. S. Tamura, Phys. Rev. B 31, 2574 (1985).
7. Y. B. Levinson in *"Physics of Phonons,"* T. Paszkiewicz ed., Springer Verlag 1987, pp.444-449.
8. W. Seidel, et al., these proceedings.

Calorimeters with Proximity-effect Thermometers and Lead and Tin Absorbers

G. Forster, K. Hallatschek, D. Wilhelm, F. Pröbst* , W. Seidel*, E. Kellner, F. v. Feilitzsch

Technische Universität München, D-80747 Garching, Germany
**Max-Planck-Institut für Physik, Föhringer Ring 6, D-80805 München, Germany*

Taking advantage of the low critical temperatures of proximity-effect phase transition thermometers, superconductors with low Debye temperatures can be used as absorber materials for calorimetric detectors. We performed experiments with lead and tin absorbers of a mass of about 1 g. The energy resolutions for 6 keV X-rays are 1000 eV and 230 eV FWHM, respectively. A model which includes the effect of both thermal and non-thermal phonons explains the measured pulse shapes. The observed heat capacity of the absorbers agrees with that given by the Debye law. A comparison of heat pulses and of radiation induced pulses shows a thermalization efficiency close to 100%. No evidence for trapping of energy as quasiparticles is observed.

1. INTRODUCTION

Low temperature calorimetric detectors are developed to achieve high energy resolution. Two fundamental mechanisms, besides the noise connected with the measurement of the temperature, are limiting the energy resolution of calorimetric detectors:

- thermodynamic fluctuations of the absorber temperature
- statistical fluctuations of the amount of heat generated by a particle interaction.

The first contribution is inherent to calorimetric detectors, but can be influenced by the choice of operating temperature and absorber heat capacity. The second contribution can be avoided if complete thermalizaton is achieved. This is difficult in most materials with low heat capacities, as they exhibit an energy gap in the electronic density of states. Electronic states excited during the particle interaction can exhibit a large lifetime and store an appreciable part of the deposited energy. To minimize the energy gap, and thereby the contribution of the statistical fluctuations to the energy resolution, we use superconductors as absorber materials.

To gather information about the response of our calorimeters to thermal phonons, we use a heater to generate heat pulses. A comparison of the pulse height of heat and radiation pulses allows to determine the amount of heat produced by a

Presented at the Fifth International Workshop on Low Temperature Detectors (LTD-5), 29 July - 3 August 1993, Berkeley, California. To be published in Journal of Low Temperature Physics.

radiation event. A difference in pulse shapes between radiation and heater pulses may be due to a different response to thermal and non-thermal phonons.

2. EXPERIMENTAL SETUP

2.1. Phase Transition Thermometer

To measure the temperature rise after a particle interaction, we use superconducting thin films operated in the transition from the normal- to the superconducting state, where the electrical resistance shows a strong dependence on temperature. The change in resistance is measured by a SQUID, which is perfectly matched to the low impedance of the thermometers. Results obtained with pure iridium phase transition thermometers and molybdenum and vanadium absorbers have been reported previously.[1]

To lower the operating temperature of the phase transition thermometer, an iridium film (thickness $\approx$ 120 nm) is covered with a gold layer (thickness $\approx$ 100 nm). The critical temperature of this bilayer is determined by the proximity effect between both films and results in a transition temperature of 27 mK. The thermometer film with a total area of 17 mm^2 is evaporated on a single crystal sapphire substrate. The transition width of the particular thermometer used for these experiments was 8 mK. Details of the fabrication of the thermometers and the dependence of the critical temperature on the properties of the films are published elsewhere in these proceedings.[2]

2.2. Calorimeters

The lead and tin absorbers are disks of $\approx$ 1 mm thickness and 12 mm diameter. The sapphire crystal (10 $\times$ 4 $\times$ 0.5 mm, mass about 80 mg), with the thermometer evaporated on top of it, is glued to the absorber with epoxy resin. Additionally, a second proximity-effect bilayer evaporated on a separate sapphire crystal with a transition temperature lower then 10 mK is also glued to the absorber crystal and used as a heater. The absorber rests on three ruby balls and is held in place by a forth spring loaded ruby tip from the top. The electrical connections were established by aluminum bonding wires of negligible thermal conductance. The thermal coupling was achieved by bonding gold wires from one end of the thermometer to the calorimeter holder. The thermal conductance of the gold wires was about 1 nW/K.

The lead absorber is a single crystal with a mass of 1.57 g. Its residual resistivity ratio was determined to be 1600. The tin absorber (mass 1.15 g) was cut from a polycrystalline piece of tin with a residual resistivity ratio of 10000.

3. LEAD CALORIMETER

3.1. Spectra

Even in the absence of an external source, high energetic pulses with a rate of 0.5 Hz are observed with the lead crystal. They are due to a contamination of the lead with ^{210}Pb of about 10^{-13} g/g. The high energy part of the observed spectrum

can be seen in figure 1a, the low energy part in figure 1b. All products of the decay

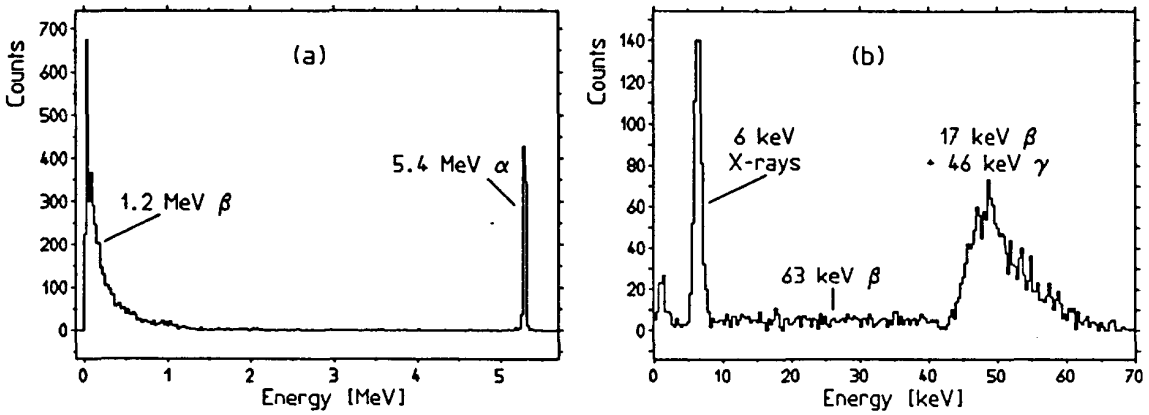

Fig. 1. **1.5 g lead absorber:** (a) High energy part of the spectrum of the decay chain of ^{210}Pb, (b) spectrum of the decay of ^{210} Pb and of a 6 keV X-ray source. The energy resolution is 1 keV FWHM for 6 keV X-rays.

chain of ^{210}Pb can be identified: The 5.4 MeV α-decay of ^{210}Po and the β-decay of ^{210}Bi with a Q-value of 1.2 MeV in figure 1a, and the decay products of ^{210}Pb in figure 1b. ^{210}Pb decays in two branches: 81 % of its β-decays end up in an excited state of ^{210}Bi, and the sum energy of the β-decay with a Q-value of 16 keV and of the 46.5 keV γ-decay are visible as a peak around 50 keV in figure 1b. 19 % of the ^{210}Pb nuclei decay into the ground state of ^{210}Bi, and the β-decays with 63 keV endpoint energy are visible as events between 6 and 45 keV. Additionally, 6 keV X-rays from an external source are resolved with an energy resolution of 1 keV FWHM.

3.2. Pulse Height

The pulse height of the 6 keV signals is 2.9 μK, in accordance with the calculated Debye heat capacity of 250 pJ/K of the lead absorber and the electronic heat capacity of 22 pJ/K of the heater and the thermometer. This observation leads to two conclusions: The heat capacity of the lead absorber is not increased over its Debye value (for example by impurities), and the thermometer measures the full temperature rise of the absorber. The reduction of the thermometer temperature rise by the competition of the thermal conductances between thermometer and absorber, respectively heat bath, is of minor importance. This is very different from the experiments with dielectric absorbers and proximity-effect thermometers discussed elsewhere in this proceedings,[3] where this effect is important.

The difference is mainly due to a different thermometer geometry. The thermal conductance between thermometer and absorber is dominated by the electron-phonon-coupling at the operating temperature of our calorimeters. As the thermometers used in our experiments possess a volume larger by a factor of five than the thermometers in the experiments with dielectric absorbers, the electron-phonon-coupling is increased correspondingly and the difference in thermometer and absorber temperature is diminished.

3.3. Position Dependence

The energy resolution of the α line is 0.5 %. As the α emitting nuclei are homogeneously distributed in the crystal, the position dependence of the detector cannot be larger than this value.

4. TIN CALORIMETER

The tin calorimeter was irradiated with K_α and K_β X-rays form a ^{55}Fe source. The resulting spectrum is illustrated in figure 2. The energy resolution is 230 eV FWHM. The observed pulse height of 14 μK is consistent with the calculated heat capacity of the phonon system of the tin absorber of 45 pJ/K and the heat capacities of thermometer and heater of 22 pJ/K.

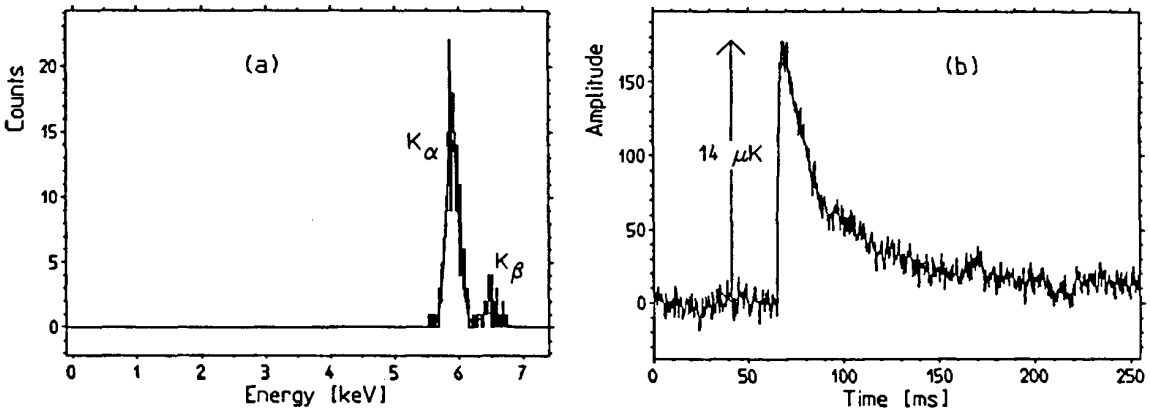

Fig. 2. **1.2 g tin absorber:** (a) Spectra of K_α and K_β X-rays from a ^{55}Fe source. The enery resolution is 230 eV FWHM. (b) Pulse shape of a single 5.9 keV event.

5. PULSE SHAPE

The observed pulse shapes consist of four exponenetial components in both calorimeters, two rise times and two decay times. Figure 2b shows an example of the pulse shape of 6 keV X-ray pulses. For the tin calorimeter, we observe two rise times with time constants of 50 μs and 1.6 ms, and two decay times with time constants of 17 ms and 160 ms. For lead, the corresponding time constants are 130 μs, 1.5 ms, 50 ms and 600 ms. The amplitude of the slow decaying component is about 10 % of the total pulse height.

The fast rise time reflects the heating of the thermometer by non-thermal phonons absorbed by the electron system of the thermometer, as described elsewhere in these proceedings[3] for dielectric absorbers. A large part of the phonons is nevertheless thermalized in the absorber and raises the absorber temperature over the thermometer temperature. The temperature relaxation between thermometer and absorber causes the second rise time. The fast decay time is due to the cooling of the phonon system of the absorber into the heat bath and an additional heat capacity, which is weakly coupled to the phonons of the absorber, giving rise to the

slow decay time. A more detailed description of these effects is given elsewhere.[4] This interpretation of the pulse shapes can be checked by using heat pulses.

6. HEAT PULSES

By means of the heater glued seperately onto the absorber crystal, thermal phonon pulses of well defined energy can be injected into the absorber. To this purpose, a sinusoidal current with a duration of about 10 μs is fed into the heater. The resulting pulse shape is similar to the shape of radiation pulses, with the exception of the rise time of about 2 ms for both calorimeters. The thermal resistance between electron and phonon system of the heater limits the time constant of the energy transfer into the absorber to this value. The two decay times are identical to the decay times of radiation pulses. Because of this, their cause cannot be the thermalization of high frequency phonons or the relaxation of metastable states, as they would not be excited by the the thermal phonons emitted from the heater.

To determine the relaxation time of the thermometer, the gold bonding wire is used as a resistive heater. A short current pulse is used to heat up the bonding wires. The heat flowing into the thermometer causes its temperature to rise over the absorber temperature, and the decay time of the resulting pulse shape gives the relaxation time of the thermometer. For the lead absorber, we obtain a time constant of 1.7 ms and for the tin absorber of 2.0 ms. The agreement with the slow rise times of the radiation pulses shows that the interpretation of the slow rise time as relaxation time of the thermometer is correct.

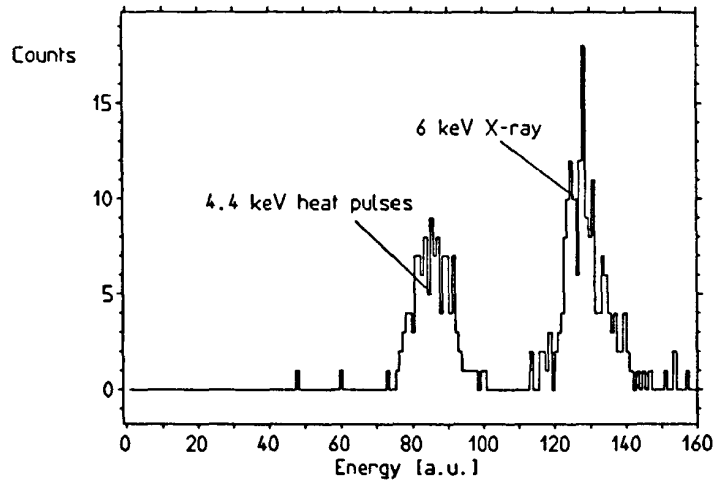

Fig. 3. Comparison of pulse heights of heat and radiation pulses. The pulse height of the heat pulses is smaller than expected from the pulse height of the radiation pulses.

The pulse height of radiation pulses compared to heat pulses can be seen in figure 3. The temperature rise of heat pulses is smaller than expected from the pulse height of the radiation pulses. The longer rise time of the heat pulses allows some heat to leak into the additional heat capacity, thereby reducing the amplitude of the

fast decaying component. A more suitable method to evaluate the thermalization efficiency is to compare the time integral of the pulses. This gives a thermalization efficiency of 110 % ± 10 % for lead and 101 % ± 3 % for tin. The errors reflect the difficulty of the determination of the value of the slow decay time constant.

7. CONCLUSION

We have obtained an energy resolution of 230 eV FWHM for 5.9 keV X-rays with a 1.2 g tin absorber. The resolution was limited by a rather wide transition of 8 mK. The position dependence is smaller than 0.5 % in the case of the lead absorber. The thermalization efficiency was determined to be 100 % for both calorimeters. The additional contribution to the energy resolution due to statistical fluctuations of the number of excited metastable states is expected to be small.

ACKNOWLEDGEMENTS

This work is supported by the Bundesministerium für Forschung und Technologie.

REFERENCES

1. G. Forster, P. Ferger, F. v. Feilitzsch and R. L. Mößbauer, Nucl. Instr. Meth. **A 324**, 491, (1993).
2. U. Nagel et al., these proceedings.
3. M. Frank et al., these proceedings.
4. G. Forster, PhD thesis, Technical University Munich, July 1993.

Physics, Fabrication, and Characterization of Thin Films

H.Kraus, M.Gutsche, J.Jochum, and B.Kemmather

Technische Universität München, Physik Department E15, 85748 Garching, Germany

Superconducting tunnel junctions as well as transition edge thermometers could benefit from high quality thin films. We point out the important features of various cryo detectors and show where high purity, or even epitaxially grown films are advantageous for detector performance. Some fabrication methods are discussed and methods of film characterization introduced. Photolithography has proven necessary to fabricate the complex structure of the present cryo detectors.

— PACS numbers: 29.40, 74.50, 74.75

I. INTRODUCTION

Among the different cryogenic detectors, many of them are based on thin film technology. There exist other concepts such as NTD Ge sensors, metastable granules, or doped Si and Ge thermistors which do not require thin metal films. In the field of tunnel junctions or thin metal films as thermometers, fabrication techniques become more and more sophisticated. Thin films play an important role in the following three main applications:

Tunnel Junctions: Tunnel junctions are thin films. The signal to noise ratio exhibited by tunnel junction detectors is affected by the lifetime of excess quasiparticles in the tunnel junction films. Epitaxial growth as well as geometry definition by photolithography could prove beneficial for the quasiparticle lifetime.

Absorber in Tunnel Junction Detectors: In superconducting absorbers competition exists between decay of excess quasiparticles and diffusion towards the attached tunnel junctions. In order to fabricate absorbers with significantly large sensitive areas, clean and pure films have to be fabricated.

Phase Transition Thermometers: The sensitivity of a phase transition thermometer is governed by the steepness of the resistance versus temperature curve at the transition between the normal and superconducting state. Very clean and reproducible films are thus desired.

II. SUPERCONDUCTING TUNNEL JUNCTIONS

Superconducting tunnel junctions consist of two superconducting metal layers separated by a thin tunnel barrier through which quasiparticles may tunnel. The tunnel current generated thereby is in many applications integrated by a charge sensitive

Presented at the Fifth International Workshop on Low Temperature Detectors (LTD-5), 29 July - 3 August 1993, Berkeley, California. To be published in Journal of Low Temperature Physics.

preamplifier, yielding a voltage signal proportional to the number of electrons tunneled. Quasiparticles are created by energy deposition in at least one film of a tunnel junction. In addition, there are thermally excited quasiparticles at finite temperature, whence low operating temperatures are advantageous for the signal to noise ratio of tunnel junction detectors.[1] The signal to noise ratio $\mathcal{R}_{SN}$ of a tunnel junction and its associated preamplifier is roughly proportional to the square root of the quasiparticle lifetime τ_V in the films of the tunnel junctions and the quality factor $\mathcal{Q} = R_D/R_{NN}$, with R_D the dynamical resistance at the bias point and R_{NN} the normal conducting resistance. $\mathcal{R}_{SN}$ is inversely proportional to the square root of the area of the tunnel junction A_t and the tunnel time constant τ_T.[2]

The dynamical resistance R_D is effectively influenced by the quality of the metal films of the tunnel junctions. Parts of the films which are very thin can become normal conducting, thereby decreasing R_D. Rough and granular films with many grain boundaries may exhibit a small demagnetization factor and the magnetic field necessary to suppress the d.c. Josephson current could cause regions of the films to become normal. Magnetic impurities also reduce R_D. Those problems could be avoided if the films for the tunnel junctions were produced under appropriate good growth conditions.

III. THIN ABSORBER FILMS

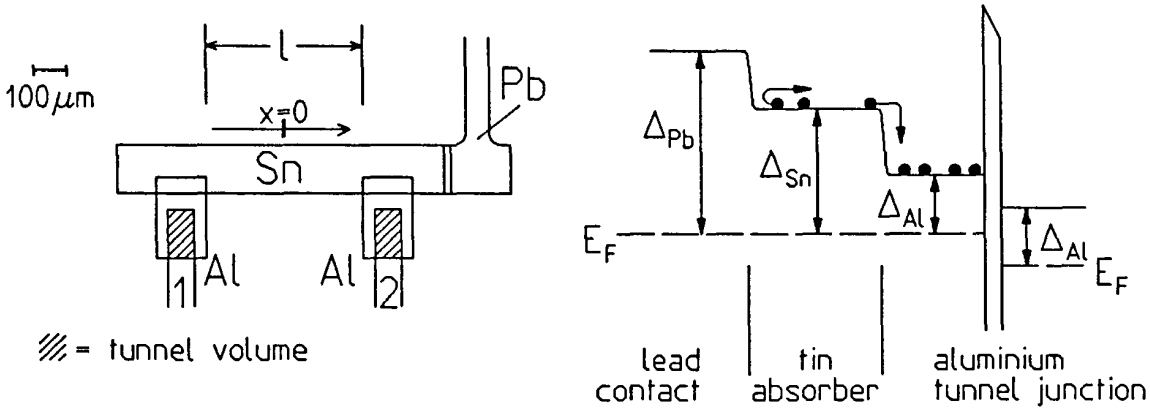

Fig.1: On the left, the geometry of an X-ray detector comprised of a Sn absorber and two Al tunnel junctions is shown. Quasiparticles created by energy deposition in the absorber diffuse therein and get trapped by one layer of the tunnel junctions. There, a fraction of them tunnels, thereby causing a charge signal. A Pb contact attached to the absorber blocks the way out for quasiparticles into the electrical common contact. The energy level diagram is shown on the right.

Fig.1 shows the arrangement of one of our detectors consisting of a superconducting absorber with two attached tunnel junctions. Quasiparticles created in the absorber propagate therein by diffusion and are subject to local trapping in small gap depressions. This local trapping is expressed by a time constant τ_D describing quasiparticle loss within the absorber.[3] The equation for the quasiparticle density

$n(x,t)$ along an absorber of length ℓ is:

$$\dot{n}(x,t) = D \cdot \Delta n(x,t) - \tau_D^{-1} \cdot n(x,t) \qquad (1)$$

D is the diffusion constant for electrons in the absorber and is proportional to the mean free path $\bar{\ell}$ of electrons in the absorber film. The measured signals are the charges $Q^{\pm}$ provided by the two tunnel junctions:

$$Q^{\pm} = E_0 \cdot \frac{C}{\omega} \cdot \frac{\sinh\alpha\left(\frac{1}{2} \pm \frac{x_0}{\ell}\right)}{\sinh\alpha} \qquad \text{with} \qquad \alpha = \frac{\ell}{\sqrt{D\tau_D}} \qquad (2)$$

The constant C, $(0 < C \leq 1)$, reflects the charge collection efficiency of the tunnel junction – preamplifier chain. The inversion of eq. 2 yields energy E_0 and position x_0 of the absorbed initial radiation.

For detectors exhibiting high energy and position resolution, the parameter α should not exceed ~ 1.5. In order to have absorbers of large length ℓ, the diffusion constant $D \propto \bar{\ell}$ and the quasiparticle lifetime in the absorber τ_D must be high, which can be achieved with high quality epitaxial absorbers. $\bar{\ell}$ and τ_D are limited by impurities, inhomogeneities, grain boundaries, or defects.

IV. MODELS FOR THE PROXIMITY EFFECT

If two metals, of which at least one is superconducting, are metallically connected, the superconducting properties of both metals are modified as a consequence of the proximity of the two metals. Several models describing the change of parameter such as critical temperature of a proximity bilayer, or the spatial variation of the energy gaps in the superconducting metals have been developed. Since the models are based upon very different assumptions and boundary conditions, e.g. dirty films – clean films, the actual experimental situation has to be carefully analyzed prior to application of a specific model.

The sensitivity of calorimetric detectors is increased if operated at lower temperatures. There is, however, a lack of applicable superconductors with transition temperatures below $T_C < 125\,\mathrm{mK}$.[4] Thus, the proximity effect can be relevant for phase transition thermometers where it is desirable to produce thermometers with selectable operating temperatures. The models developed for the application to bilayer thermometer are required to reveal the bilayer's critical temperature as a function of the single film thicknesses.

In tunnel junction detectors superconductors of different energy gaps are used. The detailed knowledge of the superconducting properties at the interface between two superconductors is of special interest for the understanding of the quasiparticle trapping process.[3,5,6] Here, the models should describe the change of the energy gap along an axis normal to the interface between the two superconductors.

No single satisfactory fundamental theory exists for proximity phenomena. Various models where developed which fit more or less for a specific problem. Some of these theories are discussed in the following:

Cooper:[7] The transition temperature T_C is intuitively expressed in terms of a spatially averaged pairing interaction. This is accomplished by a modification of

the parameter $N(0)V \longrightarrow (N(0)V)_{av}$ in the equation for the energy gap Δ.

$$\Delta = 2\,(\hbar\omega)_{av} \cdot \exp\left(-\frac{1}{(N(0)V)_{av}}\right) \tag{3}$$

The model is developed for 'clean' films which, however, are believed difficult to be achieved.

McMillan:[8] This model considers a potential barrier between the S and N metals of thicknesses d_S and d_N. It has one free parameter σ, which describes the transmission of electrons across the barrier. The metals are assumed to be thin so that the superconducting properties do not change across the metals. In such a case, the transition temperature T_C in the Anderson limit ($\Gamma_S + \Gamma_N \gg kT_{C0}$) is given by:

$$T_C \sim T_{C0} \cdot \left(\frac{k\,T_{C0} \cdot \pi}{2\gamma\,(\Gamma_N + \Gamma_S)}\right)^{\Gamma_S/\Gamma_N} \tag{4}$$

$$\text{with } \gamma = 1.781 \qquad \text{and} \qquad \Gamma_{S,N} = \frac{\hbar v_{F_{S,N}}}{2} \cdot \left(\frac{\sigma}{B\left(\frac{\bar{\ell}}{d_{S,N}}\right)}\right) \cdot \frac{1}{d_{S,N}} \tag{5}$$

T_{C0} is the transition temperature of the bulk superconductor, v_F is the Fermi velocity, and B is a dimensionless function of the ratio of the mean free path $\bar{\ell}$ to the film thickness d. It is assumed in eq. 5 that $\bar{\ell} \sim d$.

Golubov and Houwman:[6,9] SNINS and SNIS' tunnel junctions with HTSC materials where investigated. A theory describing the Josephson effect in such tunnel junctions was the initial motivation for formulating such a theory. The problem is treated in the 'dirty' limit for both N and S metals. The two conditions, with $d_{S,N}$ and $\xi_{S,N}$ the film thicknesses and coherence lengths,

$$d_S \gg \xi_S \qquad \text{and} \qquad d_N \ll \xi_N \tag{6}$$

allow to neglect the reduction of T_C in the bulk superconductor and renders all quantities within the N layer independent of the position coordinate. Two parameter γ_B and γ_m are used to characterize the proximity effect.

Hilsch and Hilsch:[10] This is a semi empirical model based on a phenomenological theory by Fröhlich. The free energy of a superconductor is compared to its reduction in a volume of thickness L by the presence of a normalconductor. It follows:

$$T_C = T_{C0} \cdot \sqrt{1 - \frac{L}{d_S}} \tag{7}$$

For superconducting metals with $\bar{\ell} \ll \xi_0$, $\xi = \sqrt{b\xi_0\bar{\ell}}$ holds, with b a constant of the BCS theory and ξ_0 the intrinsic coherence length. L is assumed to be an effective coherence length into which impurity scattering as well as surface scattering of electrons have to be included:

$$L = \frac{\sqrt{b\xi_0}}{\sqrt{\beta\left(\frac{1}{\ell_S} + \frac{1}{d_S}\right) + \gamma\left(\frac{1}{\ell_N} + \frac{1}{d_N}\right)}} \tag{8}$$

β and γ contain material properties and are the two adjustable parameter of the model.

Werthamer and de Gennes: de Gennes and Guyon[11] have formulated a theory for the 'dirty' limit under the condition that $\bar{\ell} \ll d$. The problem of the effect of a sharp SN interface is eased by the presence of impurities. Werthamer has generalized the model for $d < \xi$.[12] The model of Werthamer, de Gennes, and Guyon has in principle no free parameter. In practice, however, an 'adjustment' factor has to be included to explain the experimental results. A more detailed discussion of this model is given in ref.4.

The proximity effect models describe the superconducting behavior at the interface between a superconductor and another metal. Depending on the real experimental situation (e.g. dirty films – clean films), one of the models may prove to describe the reality best. During the fabrication process, which may be very critical in particular cases, interdiffusion between the two metals may occur or an additional oxide layer may be introduced. Both effects must be avoided.

V. FABRICATION

In order to achieve very clean epitaxial films the application of an ultra high vacuum system exhibiting MBE type vacuum conditions is indispensable. We use a VARIAN VT 109 system, equipped with turbomolecular pump, ion getter pump, titanium sublimation pump, and two liquid nitrogen panels. A base pressure of better than $2 \cdot 10^{-11}$ mbar was attained after baking the system for several hours at a temperature of 280 °C. During evaporation the pressure was maintained in the low 10^{-10} mbar range. An all-tantalum substrate heater was employed to heat the substrate up to $\sim$ 1100 °C during bake out. For evaporation, a single crucible e^--gun from VARIAN with a volume of 1.1 cm^3 was used. It was observed that vacuum distillation of the source material had a very beneficial influence on the mean free path achieved in our films.

Films were grown at substrate temperatures ranging from $\sim$ 50 °C up to 950 °C. At such high temperatures, incorporation of impurities by outgassing structural material in the vicinity of the substrate may cause a reduction of the film quality. In addition, interdiffusion between substrate material and metal film may cause a problem.

VI. CHARACTERIZATION OF FILMS

Among the criteria for film 'quality', the mean free path $\bar{\ell}$ is decisive in a variety of applications (see e.g. eq. 2). $\bar{\ell}$ is proportional to the residual resistance ratio RRR, which can be easily determined.

$$\bar{\ell} = \mathrm{RRR} \cdot \bar{\ell}_{\mathrm{intr.}} \tag{9}$$

For further characterization, additional methods discussed in the following are used. The various methods listed below are rather general and may be employed for almost any material. As we have studied vanadium films on various substrates, we discuss our measurement as an example.

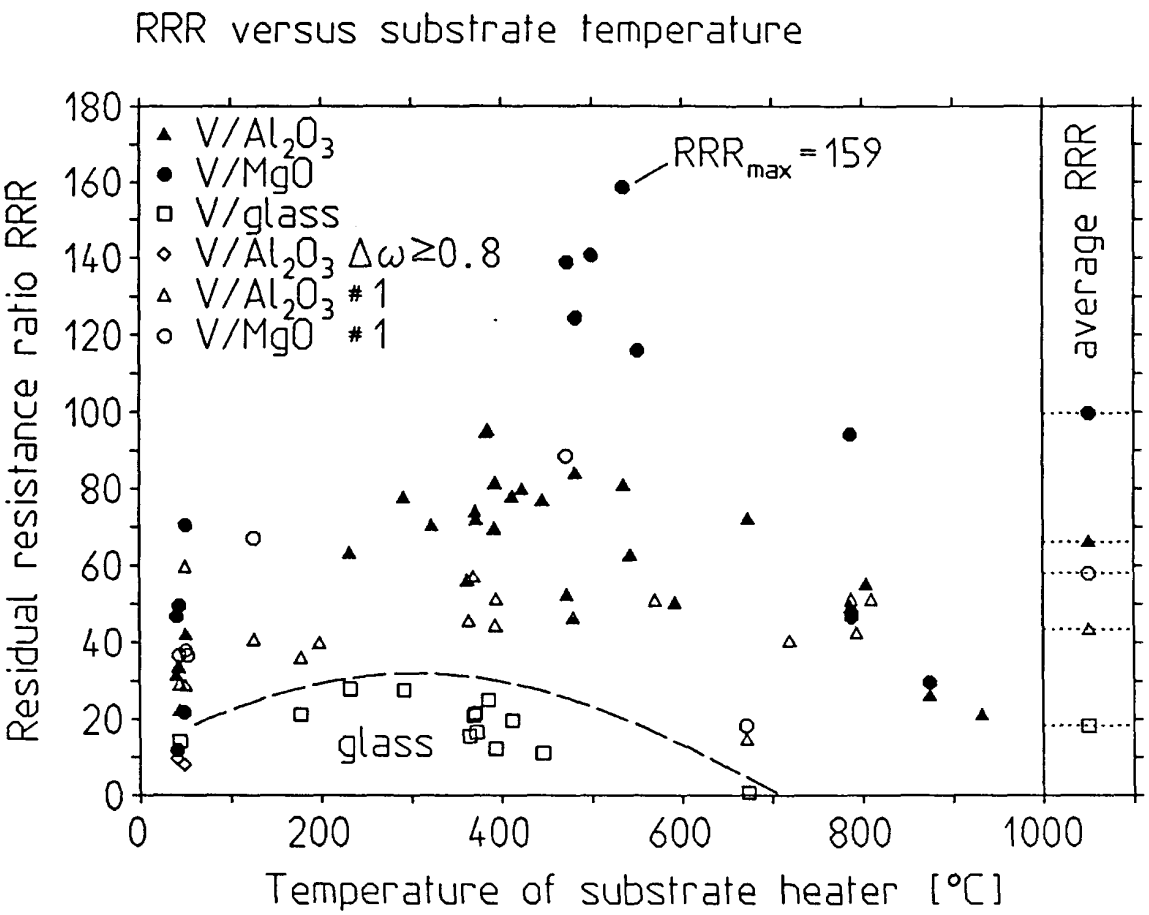

Fig.2: Residual resistance ratios for vanadium films grown on glass, MgO, and Al_2O_3 substrates versus temperature of the substrate heater during growth. The solid symbols represent films of optimal quality. No epitaxial growth is expected on glass as a substrate. Open symbols mark films with known deficiencies.

1. Residual Resistance Ratio: The residual resistance ratio is defined as $RRR = R_{298K}/R_{res} - 1$. R_{298K} and R_{res} are the resistances at room temperature and slightly above the transition from the normalconducting to the superconducting state, respectively. A crude estimate of $\bar{\ell}_{intr.}$ (see eq. 9) can be made with the help of the Drude model.

$$\bar{\ell}_{intr.} = \frac{m^* v_F}{\rho_{298K} n e^2} \tag{10}$$

m^*, v_F, ρ_{298K}, n, and e are the effective electron mass, Fermi velocity, specific resistance at room temperature, electron density, and electronic charge, respectively. $\bar{\ell}$ may also be limited by surface scattering in films of thickness d. This effect may be employed to determine $\bar{\ell}_{intr.}$ experimentally.[13]

$$\sigma_{film} = \sigma_{bulk} \cdot \left(1 - \frac{3}{8}\frac{\bar{\ell}_{intr.}}{d}\right) \tag{11}$$

The values for $\bar{\ell}_{intr.}$ range from 18 Å to 57 Å for our vanadium films depending on the method of determining $\bar{\ell}_{intr.}$. We use an average value of $\bar{\ell}_{intr.} = 40$ Å.

Vanadium has been grown on glass, Al_2O_3, and MgO substrates. Values of RRR < 30 were obtained for vanadium on glass, where no epitaxial growth is expected. The average RRR for vanadium grown on Al_2O_3 was higher by a factor of 3.3 compared to vanadium grown on glass. MgO as substrate gave mean RRR values 1.5 times higher than with Al_2O_3 as substrates. The optimal RRR of 159 was obtained with MgO substrates at a growth temperature of 535°C (see fig.2). A mean free path of ~ 6400 Å results if $\bar{\ell}_{\text{intr.}} = 40$ Å is used. Still, at low growth temperatures ($T_S \sim 50\,°C$) good values of RRR (~ 70) were attained for V on MgO, while at very high temperatures ($T_S > 850\,°C$) RRR decreased below ~ 10. This decrease may be attributed to a higher impurity content in the films due to outgassing of material in the growth chamber. In addition, interdiffusion between substrate and metal film may pose a problem.

2. Bragg law: X-ray diffraction is used to determine the epitaxial relationship between the substrate and the film. We have used a conventional Bragg–Brentano geometry with Cu K_α radiation as X-ray source. The data indicate epitaxial growth of vanadium on both MgO (100) and Al_2O_3 ($\bar{1}012$) substrates. The Bragg angle can be measured in a θ–2θ scan. The lattice parameter determined thereby is 3.022 Å for our V on Al_2O_3 and 3.031 Å for our V on MgO. The bulk value for vanadium is 3.024 Å.

3. Scherrer formula: In the θ–2θ scans of V (002) peak widths of less than $\Delta(2\theta) = 0.1°$ have been achieved for growth temperatures of $T_S > 200\,°C$ on both MgO and Al_2O_3 substrates. Using Scherrer's formula for particle-size broadening, we estimate the crystallite size in growth direction to be larger than ~ 1000 Å in our best vanadium films.

4. Rocking curve: The sample is rocking while the incident X-ray beam and the detector are at fixed positions. The tilt of single crystallites within the film can be determined from the width $\Delta\omega$ of the peak in the rocking curve. Values as low as $\Delta\omega = 0.2°$ are obtained for growth temperatures of $\sim 200\,°C$. Below $T_S < 200\,°C$ rocking curve width were typically $\sim 0.4°$. $\Delta\omega \approx 14°$ and a pronounced reduction in intensity is the result for vanadium on glass.

5. Φ scan: The sample is rotated with respect to an axis normal to the film surface. The four–fold symmetry of the V (202) reflection was indeed measured. Caused by the special orientation of our substrates, the first peak in the Φ scan spectrum was at position 45° and the four peaks were indeed spaced by 90°.

6. Orientation of V on Al_2O_3: Three dimensional growth of vanadium causes a tilt of the vanadium (002) plane with respect to the Al_2O_3 ($\bar{1}012$) substrate surface by $\sim 3°$ in our case. Fig.3 shows a cross section in which the c-axis of Al_2O_3, the axis with the highest symmetry, is visible. The axis with the corresponding three-fold symmetry in vanadium is the V ⟨111⟩ direction. In order to align these two axes, the vanadium (001) plane has to grow tilted by 2.87°. Such a behavior of our samples is indeed observed.

7. RHEED: Reflection High Energy Electron Diffraction also gives information on the lattice constant of the material grown. The advantage of RHEED is that it is nondestructive and may be employed in the growth chamber to provide in-situ monitoring of the latest layer grown.

8. RBS: Rutherford Back Scattering in combination with channeling gave infor-

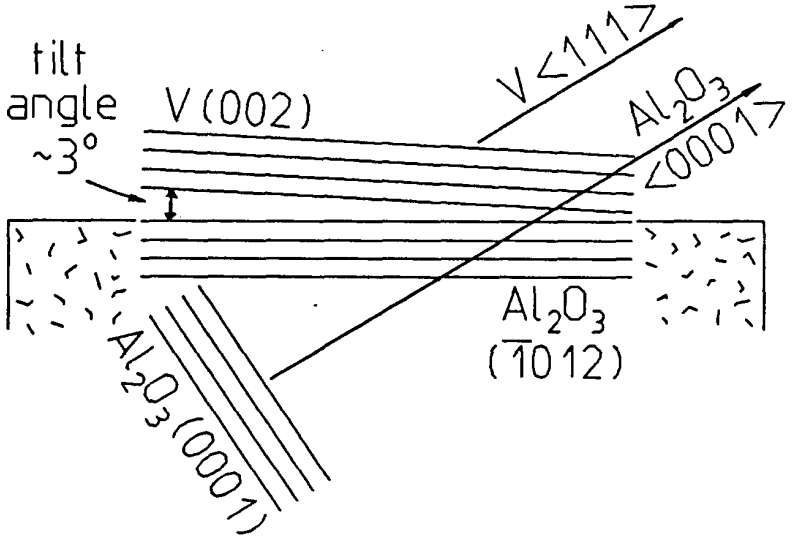

Fig.3: Three dimensional oriented growth of vanadium on top of the sapphire $(\bar{1}012)$ plane. The sapphire c-axis $\langle 0001 \rangle$ exhibits the highest symmetry and is tilted against the $(\bar{1}012)$ plane by 57.6°. The axis with the corresponding three-fold symmetry in the vanadium is the $\langle 111 \rangle$ axis. If growth of the vanadium on sapphire is aligned such that V < 111 > and Al_2O_3 < 0001 > are parallel, V(002) is tilted by 2.87° against $Al_2O_3(\bar{1}012)$.

mation on the crystal perfection of our samples. α particles with an incident energy of 1.6 MeV were used and the back scattered He^{++} ions were recorded at an angle of 170°. For our vanadium films, the minimum scattering yield was in good agreement with the theoretical prediction for bulk vanadium.

9. AFM: An Atomic Force Microscope may be used to distinguish between the different types of crystal growth. Growth of a film may start layer by layer (Frank–van der Merwe), by island formation (Volmer–Weber), or by a combination of both (Stranski–Krastanov).

10. SIMS: Secondary Ion Mass Spectroscopy permits the recording of a depth profile of impurities. The method is destructive since the sample is exposed to a primary ion beam sputtering off secondary ions. These secondary ions are registered by a mass spectrometer. The sensitivity of this method is of order ppm to ppb. Quantitative statements are difficult due to strongly varying ionization probabilities and sensitivities for the different ions. SNMS (secondary neutral mass spectroscopy) is a method which is less sensitive, but permits quantitative measurements.

11. TEM: Transmission Electron Microscopy permits the investigation of films and interfaces on an atomic scale. For our vanadium films the interface to the substrate is clearly flat and abrupt. The epitaxial relationship between vanadium and sapphire is characterized by a semi-coherent interface with misfit dislocations accommodating the mismatch between the vanadium and sapphire lattices. The HRTEM studies were performed at the Max-Planck-Institut in Stuttgart.

12. Influence of impurities on T_C: The transition temperature T_C of a superconducting film was found to depend on film thickness d and on the mean free

path $\bar{\ell}$. The influence of the film thickness was investigated with samples of very high residual resistance ratio. According to a model of Cooper, T_C should decrease linearly with decreasing film thickness.

$$T_C(d) \approx T_{C0} \cdot \left(1 - \frac{2\,b}{NVd}\right) \tag{12}$$

T_{C0} is the bulk transition temperature and NV is the bulk interaction potential, with NV = 0.24 in the case of vanadium. b is a parameter of the BCS theory.

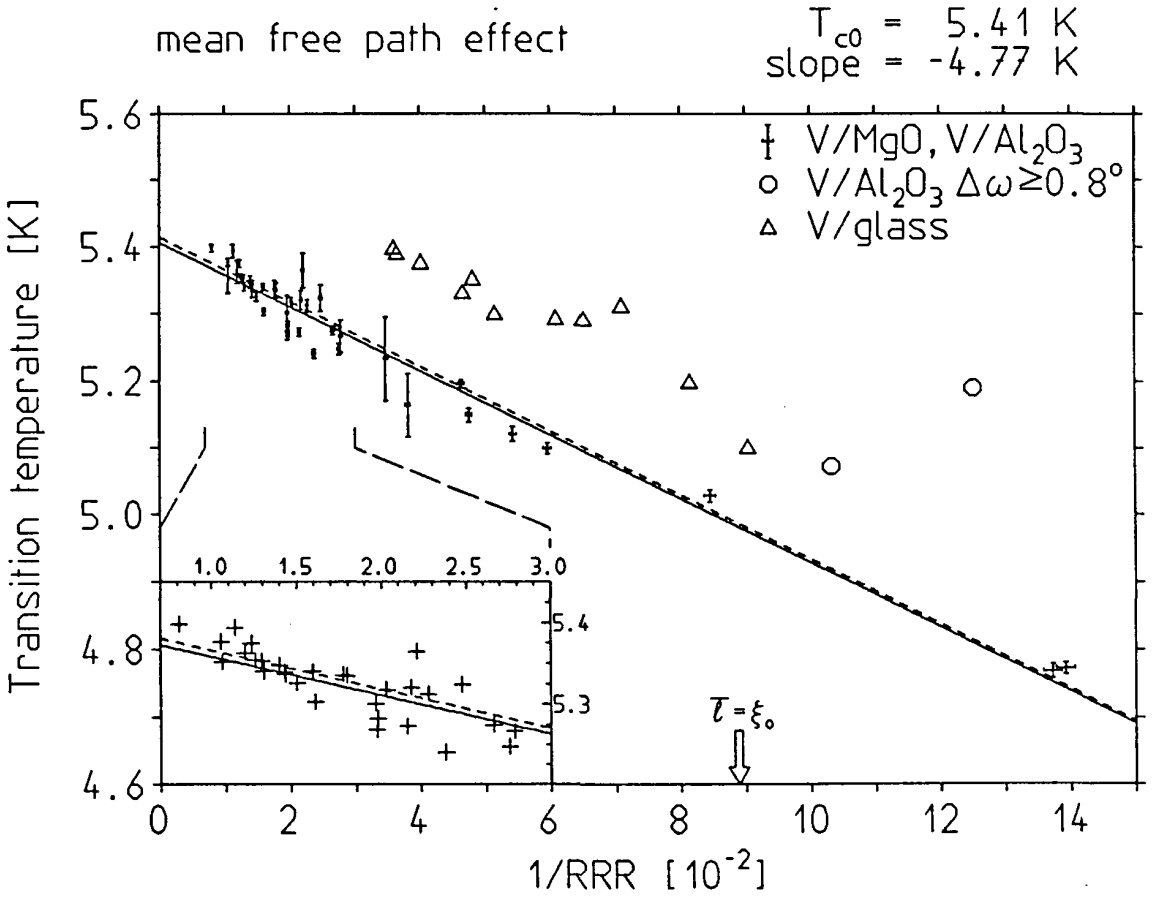

Fig.4: Transition temperature as a function of the inverse residual resistance ratio. 1/RRR is proportional to $1/\bar{\ell}$. With the long mean free paths obtained in our clean films, the dependence of T_C on $\bar{\ell}$ may be approximated by a linear function. Our vanadium films on MgO and Al_2O_3 substrates (solid line) exhibit properties close to those of bulk vanadium (dashed line). Data for bulk vanadium are taken from ref.14. Vanadium on glass shows a strong deviation from bulk material, likewise the two films with very broad rocking curve peaks.

Fig.4 represents a plot of T_C as a function of the inverse residual resistance ratio 1/RRR. In the 'clean' limit, where the decrease of the critical temperature is independent of the type of impurity, T_C decreases linearly with 1/RRR.[15]

$$T_C(RRR^{-1}) = T_{C0} \cdot \left(1 - \frac{55.76\,\langle\alpha^2\rangle}{RRR}\right) \tag{13}$$

$\langle\alpha^2\rangle$ is the mean square deviation of the energy gap. It may be clearly seen in fig.4 that the results for our vanadium films on MgO and Al_2O_3 substrates exhibit bulk material properties. Vanadium on glass, where no epitaxial growth is expected, shows a strong deviation from the straight line defined by equation 13.

VII. SUMMARY

High quality thin films are important for a variety of cryo detectors. Vanadium epitaxial absorbers have been fabricated with a mean free path of $\bar{\ell} \approx 6400\,\text{Å}$. This permits absorber sizes in X-ray detectors of some mm^2. Tunnel junctions themselves are at present mostly fabricated with amorphous films. Although the quality is satisfactory, application of epitaxial growth and photolithography could be advantageous. A variety of models exist describing the proximity effect between two metals. None of these theories is really satisfactory.

This work is supported by the Bundesministerium für Forschung und Technologie.

REFERENCES

[1] H. Kraus et al., Nucl. Instr. Meth. **A 326** (1993) 172

[2] J. Jochum et al., "Signal to Noise...", these proceedings

[3] H. Kraus et al., Phys. Lett. **B 231** (1989) 195

[4] U. Nagel et al., "Iridium–gold proximity...", these proceedings

[5] D.J. Glodie et al., Phys. Rev. Lett. **64** (1990) 954

[6] P.A.J. de Korte et al., in: EUV, X-Ray, and Gamma-Ray Instrumentation for Astronomy III, Oswald H. W. Siegmund, Editor, Proc. SPIE 1743 (1992) 24

[7] L.N. Cooper, Phys. Rev. Lett. **6** (1961) 689

[8] W.L. McMillan, Phys. Rev. **175** (1968) 537

[9] A.A. Golubov and M.Yu. Kupriyanov, Sov. Phys. JETP **69**(4) (1989) 805

[10] P. Hilsch and R. Hilsch, Zeitschrift für Physik **180** (1964) 10

[11] P.G. de Gennes and E. Guyon, Phys. Lett. **3** (1963) 168

[12] N.R. Werthamer, Phys. Rev. **132** (1963) 2440

[13] E.H. Sondheimer, Adv. Physics **1** (1952) 1

[14] R. Radebaugh and P.H. Keesom, Phys. Rev. **149** (1966) 209

[15] D. Markowitz and L.P. Kadonoff, Phys. Rev. **131** (1963) 563

Superconducting Tungsten Films for Use as Phase Transition Thermometers for Calorimetric Detectors

P. Colling, A. Nucciotti, W. Seidel, F. Pröbst, S. Cooper, D. Dummer, P. Ferger, M. Frank, J. Igalson, U. Nagel, A. Rulofs, and L. Stodolsky

Max-Planck-Institut für Physik, Föhringer Ring 6, D-80805 Munich, Germany

To improve the sensitivity of calorimetric particle detectors we want to produce low-T_c superconducting thin films to be used as phase transition thermometers. We have succeeded in depositing epitaxial α-tungsten films on sapphire which have critical temperatures T_c near 15 mK. To our knowledge this is the first time that the T_c of bulk tungsten has been observed in thin films. Such a film has been produced on a 4 g sapphire crystal and operated as a calorimeter, giving an energy resolution of 75 eV (FWHM) for 1.5 keV X-rays.

1. INTRODUCTION

We are developing calorimetric particle detectors with superconducting phase transition thermometers, as described by M. Frank at this conference.[1] The thermometer is a small thin film of a superconductor evaporated directly onto one surface of the absorber crystal. The operating temperature of the calorimeter is set within the narrow temperature region of the superconducting-to-normal transition of the film. Here a small temperature change leads to a relatively large change in the resistance of the film, making it a very sensitive thermometer. In order to take advantage of the decrease of specific heats towards lower temperatures, we need superconducting films with low transition temperatures T_c. In this paper we report on the development of tungsten thermometers working in the temperature range near the $T_c = 15\,\mathrm{mK}$ of bulk tungsten.[2]

2. PROPERTIES OF TUNGSTEN

2.1. Tungsten as a superconductor

The superconducting transition of tungsten was first observed in 1964 by Gibson and Hein.[3] Later other groups confirmed the appearance of superconductivity in tungsten, but with a large scatter in the observed T_c's.[4] This behaviour showed the extreme sensitivity of tungsten to impurities as well as the importance of supercooling and superheating effects, which are more pronounced for lower T_c materials.

Presented at the Fifth International Workshop on Low Temperature Detectors (LTD-5), 29 July - 3 August 1993, Berkeley, California. To be published in Journal of Low Temperature Physics.

From other superconductors it is known[5] that magnetic impurities in concentrations of a part per million (1 ppm) can reduce T_c's by 1 to 10 mK. This means that for tungsten with its $T_c = 15\,\mathrm{mK}$ a few ppm of magnetic impurities can suppress superconductivity completely. Therefore extreme care must be taken during film preparation: the substrate heating system and holder, where high temperatures prevail during film deposition, should be constructed out of non-magnetic materials. During measurements of the superconducting transition temperature good magnetic shielding is needed to avoid supercooling effects or even complete suppression of superconductivity.

2.2. Crystal structure and its influence on superconductivity

The structural properties of tungsten are also strongly affected by impurities. Whereas pure tungsten in bulk crystallizes in a b.c.c. structure known as α-W, other structures are stabilized by the presence of impurities. Thin films of tungsten have been found in three different crystal structures,[6] which have different lattice constants a and superconducting transition temperatures T_c: α-W with $a = 3.165\,\text{Å}$ and $T_c = 15\,\mathrm{mK}$, β-W with $a = 5.08\,\text{Å}$ and $T_c = 1$ to $4\,\mathrm{K}$, and γ-W with $a \approx 4.2\,\text{Å}$ and $T_c \approx 4.6\,\mathrm{K}$. Since we want to operate our calorimeters at the lowest possible temperature, we want to produce only α-W.

3. FILM PREPARATION

3.1. Material selection

A tungsten single crystal (from *Johnson and Matthey*) of diameter 9 mm, length 100 mm, and purity 99.999% was used as the evaporation material. The measured residual resistivity ratio of the crystal was about 21 000. Its transition temperature was determined by placing it in a coil and measuring the change in the coil's self-inductance, giving $T_c \approx 16\,\mathrm{mK}$. The crystal was then cut by spark erosion into shorter disks and etched in a $HF+HNO_3$ solution before being placed in the water-cooled copper crucible of the electron-beam evaporator.

There are several demands on the absorber material of a calorimeter: a low specific heat capacity, a high melting temperature to avoid interdiffusion, and the presence of nuclear spin to test for a possible spin-dependent WIMP interaction in a dark matter search. These can be satisfied by sapphire (α-Al_2O_3), which has $\Theta_{Debye} \approx 1000$ K, $T_{melt} \approx 2310$ K, and spin 5/2 for the Al nuclei. Therefore we used Czochralski-grown single crystals of sapphire (from *Union Carbide* or *KCO*) as substrate material.

3.2. Epitaxy and substrate orientation

To favor the growth of the b.c.c. lattice of α-W we have tried to achieve epitaxial growth. Epitaxial growth of α-W has been observed on selected planes of sapphire where the misfit is small.[7] For this reason we chose the $(1\bar{1}02)$ plane or "r-plane" of sapphire. The expected epitaxial growth for α-W on this sapphire orientation is with the W (001) plane parallel to the Al_2O_3 $(1\bar{1}02)$ plane and the W [110] direction parallel to the Al_2O_3 $[11\bar{2}0]$ direction (Fig. 1).

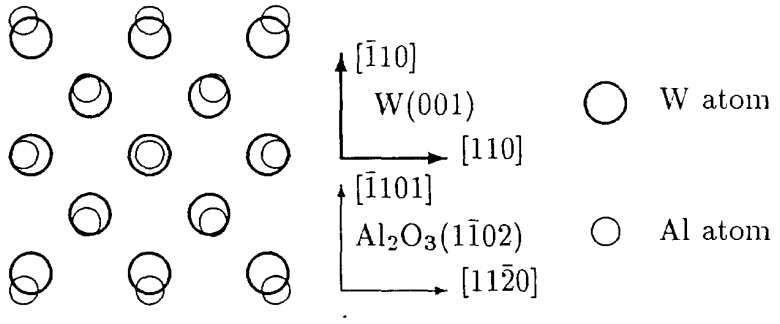

Fig. 1: Epitaxial growth of (001) α-W on (1$\bar{1}$02) α-Al_2O_3.

3.3. Deposition process

The films were prepared by electron-beam evaporation in a dedicated ultra-high vacuum system equipped with a turbomolecular pump and a liquid-nitrogen-cooled titanium sublimation pump. After a bake-out period of 24 h at 220 °C the system reaches a base pressure of 6×10^{-12} mbar. The substrate holder and electron beam evaporator are surrounded by liquid-nitrogen-cooled radiation shields. During evaporation at a rate of 2 Å/s a pressure of better than 8×10^{-10} mbar is maintained. The sapphire substrates lie in a tungsten holder and heating is provided from the back side by passing current through a tungsten sheet. The substrate temperature T_{sub} is measured by a Rh/Pt thermocouple on the holder and can be controlled in a range between 200 and 1100 °C. With this system films of thicknesses between 2400 and 6000 Å were evaporated with T_{sub} ranging from 200 to 1100 °C.

4. FILM CHARACTERIZATION

4.1. Crystal structure

The crystal structure of the films has been analyzed by a Bragg-Brentano X-ray diffractometer with a wavelength of 1.54 Å. In θ-2θ scans the incident X-ray beam and the detected, reflected beam are both at angles θ relative to the plane of the substrate, and only reflections from crystal planes parallel to the substrate surface can be seen. In all evaporated tungsten films only the b.c.c. structure was detected with a mean lattice constant of 3.167±0.002 Å. No evidence was found for the presence of β or γ-W. For $T_{sub} > 500$ °C the expected epitaxial growth (001) W || (1$\bar{1}$02) α-Al_2O_3 was observed. Only the reflection at the angle expected for the (002) reflection from the (001) plane of α-W was detected (Fig. 2 a). To confirm epitaxy and check the relationship of the directions in the substrate plane a φ-scan on the {202} planes of α-W around an axis perpendicular to the substrate surface was performed (Fig. 2 b). Only the four reflections of the {202} planes are detected. The [100] direction of tungsten is observed to be rotated by 45 degrees with respect to the [11$\bar{2}$0] direction of sapphire.

With increasing T_{sub} the crystalline structure of the films improved. This is seen from the increase in intensity of the (002) α-W reflection in the θ-2θ scans as

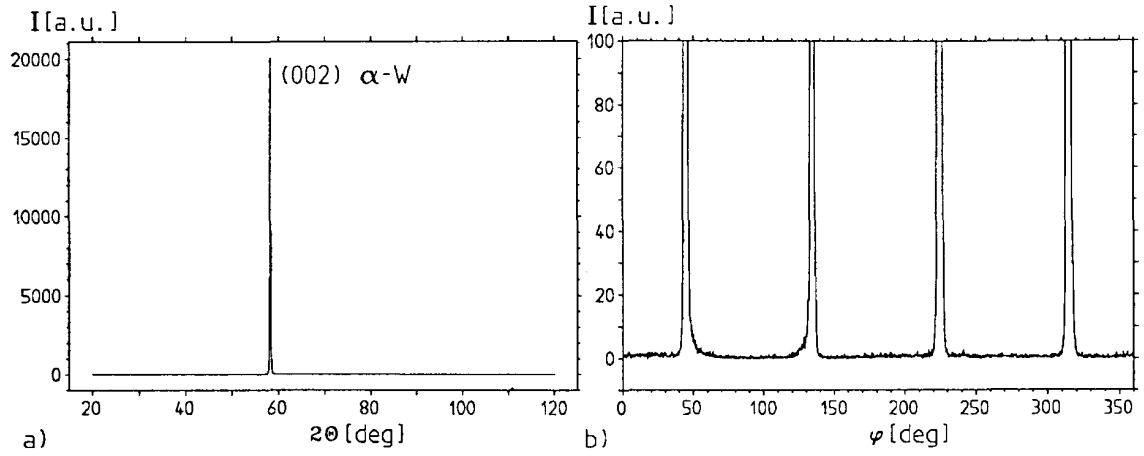

Fig. 2: a) θ-2θ-scan of tungsten film of thickness 2500 Å evaporated at a substrate temperature T_{sub} of 500 °C. Only the (002) reflection of α-W at $2\theta = 58.258$ degrees is observed. b) φ-scan on the {202} planes of the same film. $\varphi = 0$ degrees corresponds to the $[11\bar{2}0]$ direction of the sapphire substrate. The four reflections are due to the {202} planes of α-W.

well as from the increase of the residual resistivity ratio from a value of 2 to more than 21 at the highest substrate temperatures.

4.2. Superconductivity

For superconductivity measurements the films are mounted in a specially designed copper holder that is screwed directly onto the mixing chamber of a ^{3}He/^{4}He dilution refrigerator and can be cooled down to 8 mK. It is magnetically shielded by a double layer of Kryoperm. The temperature is measured with a calibrated carbon resistor. Electrical contact to the films is provided by indium press contacts and the film's resistance is measured with a lock-in amplifier using a four-point AC read-out. The superconducting transition of the film of Fig. 2 is shown in Fig. 3 a. To our knowledge this is the first measured superconducting transition at 15 mK of a tungsten film.

Films evaporated at $T_{sub} > 700$ °C had transitions at lower temperatures or showed no superconductivity at all down to 8 mK. Secondary-ion mass spectrometry (SIMS) analyses performed on these films detected a Fe, Cr and Ni contamination concentrated at the substrate-film interface. We believe that these magnetic impurities come from inside the evaporation system and are increasingly released when higher temperatures are used during preparation of the films.

5. FIRST DETECTOR WITH TUNGSTEN THERMOMETER

A tungsten film of thickness 2500 Å has been evaporated at 500 °C on a 4 g sapphire absorber crystal ($20\times10\times5$ mm^3) to test the behaviour of these new thermometers in a calorimetric particle detector. After evaporation the film was structured into a rectangular shape (6×3 mm^2) by photolithography and wet chemical etching (solution of H_2O+$K_3Fe(CN)_6$+$C_2H_8N_2$+HCl at pH $\approx$ 8).[8] A gold con-

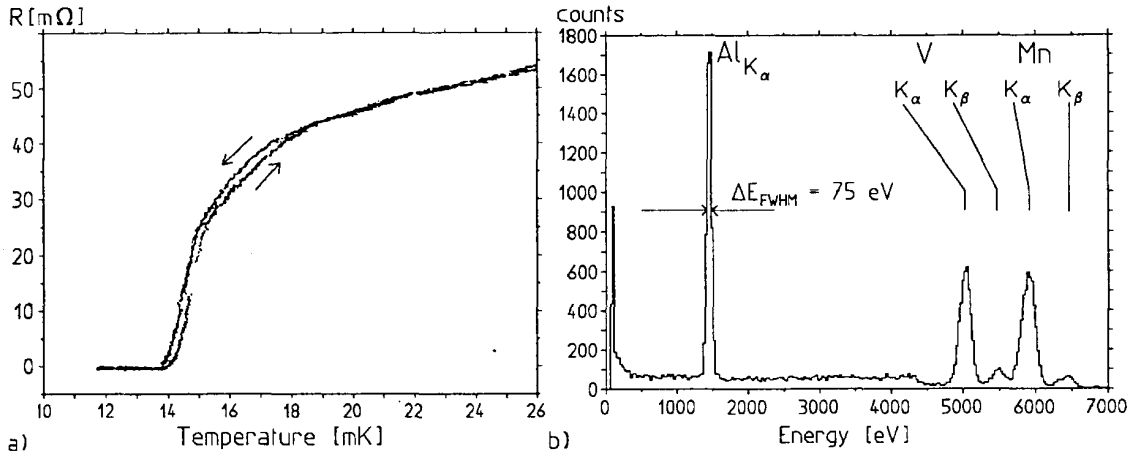

Fig. 3: a) Superconducting transition of film from Fig. 2 measured with I_{rms} = 4 μA. There is a slight hysteresis due to the time constant of the carbon thermometer. The left curve was measured while cooling down, the right one while warming up. b) Energy spectrum after optimal filtering of a 4 g sapphire crystal with tungsten thermometer when irradiated with a fluorescence X-ray source.

tact pad ($3\times0.3\times4\cdot10^{-4}$ mm^3) was deposited at each end of the thermometer in a sputter system using a lift-off technique. The calorimeter was then mounted in a dilution refrigerator, with the crystal resting on sapphire balls in a copper housing. The thermal contact between the thermometer and the housing was provided by bonding gold wires to one of the two gold pads, while the electrical contact to the read-out circuit was made with superconducting aluminium bonding wires of negligible thermal conductance. The read-out circuit consists of two parallel branches: one contains the thermometer and the other the series combination of a resistor (typically 50 mΩ) and the input coil of a SQUID. A constant current is fed through this circuit so that a change in the thermometer resistance causes a change of the current through the SQUID input coil.[9]

The copper housing was weakly coupled to the mixing chamber of the cryostat and stabilized at the working temperature using a NTD-Ge thermometer and a resistive heater. The superconducting phase transition of this film was found to be somewhat wider ($\sim$ 4 mK) than that of another film evaporated in the same run. It is not yet clear if this is caused by the photolithography process, the contact pads or unavoidable differences between films.

To test the energy response of the detector at different energies we use the fluorescence X-rays emitted by a $_{13}$Al/$_{23}$V composite target irradiated with a ^{55}Fe source. We could therefore study the energy resolution at 1.487 keV (Al$_{K\alpha}$), 4.950 keV (V$_{K\alpha}$), 5.427 keV (V$_{K\beta}$), 5.895 keV (Mn$_{K\alpha}$) and 6.490 keV (Mn$_{K\beta}$). The X-ray rate is fixed to about 1 Hz by a 1.5 mm diameter collimator. In Fig. 3 b the energy spectrum recorded with the holder at 9 mK and using a read-out current of 27 μA is shown.

Optimal shaping gives a FWHM energy resolution of 75 eV at 1.487 keV, 185 eV at 4.950 keV and 213 eV at 5.895 keV. The energy threshold is about 100 eV, and from the baseline width of roughly 50 eV a temperature resolution of about

0.3 μK can be inferred. Further studies to understand the pulse shape, the energy dependence of the energy resolution, and the limiting factors to the resolution itself are in progress.

6. CONCLUSION

We have succeeded in producing α-tungsten films with a superconducting transitions near the $T_c = 15\,\mathrm{mK}$ of bulk tungsten. With such a thermometer on a 4 g sapphire single crystal an energy resolution of $\Delta E_{FWHM} = 75$ eV for 1.5 keV X-rays has been achieved.

ACKNOWLEDGEMENTS

We thank our colleagues at the Technical University of Munich for providing space for our evaporation system and E. Kellner for his technical support. The X-ray analysis was performed by G. Neff. The photolithographic masks were made by A. Köck and his group. We thank the workshop of our institute for their excellent work in building the dilution refrigerator. The temperature control of the sample holder in the dilution refrigerator was performed using an NTD-Ge thermometer supplied by E. Haller, and other thermometers were supplied by K. Neumaier.

REFERENCES

1. M. Frank *et al.*, these proceedings.
2. P. Colling, diploma thesis, MPI preprint MPI-PhE/92-10 (1992).
3. J. W. Gibson and R. A. Hein, *Phys. Rev. Lett.* **12**, 688 (1964).
4. R. T. Johnson, O. E. Vilches, and J. C. Wheatley, *Phys. Rev. Lett.* **16**, 101 (1965); W. C. Black, R. T. Johnson, and J.C. Wheatley, *J. of Low Temp. Phys.* **1**, 641 (1969); B. B. Triplett *et al.*, *J. Low Temp. Phys.* **12**, 499 (1973).
5. G. Boate, G. Gallinaro, and C. Rizzuto, *Phys. Rev.* **148**, 353 (1966).
6. M. Gasgnier, L. Nevot, P. Baillif, and J. Bardolle, *Phys. Stat. Sol. (a)* **79**, 531 (1983).
7. A. Miller, H. M. Manasevit, D. H. Forbes, and I. B. Cadoff, *J. Appl. Phys.* **37**, 2921 (1966); J.H. Soulk, A. Segmüller, and J. Angilello, *J. Appl. Phys.* **62**, 509 (1987).
8. T. A. Shankoff, E. A. Chandross, *J. Electrochem. Soc.* **122**, 294 (1975).
9. F. Pröbst *et al.* in *"Low temperature Particle Detectors for Neutrinos and Dark Matter IV"*, Oxford, UK, September 4-7, 1991. N. Booth, G. Salmon, eds., Editions Frontières, Gif-sur-Yvette, France (1992).

Use of Proximity Effect in Iridium-Gold Superconducting Phase Transition Thermometers

U. Nagel, A. Nowak, E. Kellner,* H.-J. Gebauer, P. Colling, S. Cooper, D. Dummer, P. Ferger, M. Frank, P. Freund, G. Forster,* J. Igalson, A. Nucciotti, F. Pröbst, A. Rulofs, W. Seidel, and L. Stodolsky

Max-Planck-Institut für Physik, Föhringer Ring 6, D-80805 München, Germany
** Technische Universität München, D-85747 Garching, Germany*

We have studied the proximity effect in bilayers of thin films of iridium covered by gold. These structures were evaporated onto sapphire single crystals for use as phase transition thermometers in cryogenic particle detectors. By varying the thicknesses of the iridium and gold layers, we achieved critical temperatures as low as 33 mK. The critical temperature of the bilayers is lower than predicted by the theory of de Gennes-Werthamer, but adding a free parameter to the theory allows good agreement. The transitions of the bilayers typically had widths of a few mK, with the narrowest reaching 0.2 mK, and were always sharper than those of pure iridium films evaporated simultaneously.

1. INTRODUCTION

We are developing superconducting phase transition thermometers for calorimetric particle detectors.[1] The thermometer is a small film of superconducting material evaporated onto an absorber crystal. The basic idea is to measure the temperature rise of the film after energy is deposited by a particle interaction in the absorber. The detector is operated near the critical temperature T_c of the film within the width ΔT_c of its transition between superconducting and normal states. The strong temperature dependence of the film's electrical resistance in this region makes it a very sensitive thermometer.

Since the heat capacities of most materials decrease with temperature, it is advantageous to operate the detector at the lowest possible temperature. There are only a few superconductors with critical temperatures that are low but still easily accessible with ^{3}He-^{4}He dilution refrigerators.

In this paper we describe our use of the proximity effect[2] to reduce the T_c of iridium below its usual value of 112.5 mK by overlaying the iridium with gold. Our results on the measured T_c of iridium-gold bilayers as a function of the thicknesses of the two layers are presented and compared to theoretical calculations.

Presented at the Fifth International Workshop on Low Temperature Detectors (LTD-5), 29 July - 3 August 1993, Berkeley, California. To be published in Journal of Low Temperature Physics.

2. PREPARATION AND MEASUREMENT OF FILMS

The iridium and gold films were produced by electron-beam evaporation in a vacuum system from *Varian* (VT 109). The base pressure was 2×10^{-9} mbar; during evaporation the pressure was an order of magnitude higher. A liquid-nitrogen-cooled screen surrounded the crucibles to reduce the contamination of the films. A tantalum shadow mask was used to produce the films at the desired places on the substrate. The shadow mask and the crucibles could be moved without opening the system between the evaporation of the iridium and the gold. A water-cooled quartz crystal was used to control the deposited thicknesses.

Usually the iridium film was deposited first, with the substrate heated to between 500 °C and 600 °C. The gold film was deposited after cooling the substrate to room temperature in order to minimize interdiffusion of the gold and iridium. The iridium film was fully covered by the gold film. For diagnostic purposes single layers of iridium and gold were also evaporated on the substrate during the deposition of the bilayer.

During three runs the gold film was deposited first at a substrate temperature of 150 ± 10 °C and the iridium film second with the substrate at room temperature. In these cases the diagnostic iridium films, deposited directly on the substrates, were of poor quality with high resistivity and low residual resistivity ratio $RRR \equiv \rho_{300}/\rho_4$. However it is likely that the iridium of the bilayer, deposited on top of the gold, is of better quality.

Single crystals of 99.999 % purity sapphire from *Union Carbide* or *KCO* were used as substrates. The films of size $1 \times 7\,\mathrm{mm}^2$ were evaporated onto the highly polished $(1\bar{1}02)$ plane of the $10 \times 20 \times 1\,\mathrm{mm}^3$ crystals.

We used 99.999 % purity iridium powder (from *Johnson and Matthey*) and 99.999 % purity gold wires (from *Degussa*). Usually the powder was compressed and then melted with an electron beam in a separate vacuum system to prepare pills for evaporation. The last few films were made with high purity single crystals of iridium from *BEC Breznikar*.

The film thickness was determined by a mechanical thickness measurement device Alpha-Step 250 from *Tencor Instruments* with an accuracy of 10 Å. Measurement of a few films at different positions along the film indicated that the film thickness was typically constant within $\Delta d \approx 50$ Å.

The temperature dependence of the resistance of each film was measured in a small ^{3}He-^{4}He dilution refrigerator with a base temperature of 30 mK. The film resistance was measured with a lock-in amplifier using a current of $1\,\mu$A. The temperature where the film resistance had decreased to 50 % of its normal-conducting value was taken as the critical temperature $T_c \equiv T(50\,\%)$ and the width of the transition as $\Delta T_c \equiv T(90\,\%) - T(10\,\%)$. We also measured the critical temperatures T_{cs} of the corresponding diagnostic iridium films. The systematic error in the measurement of the critical temperatures was 1 mK.

The T_{cs} of the diagnostic iridium films varied from run to run, with most of the values clustered between 90 and 120 mK, but some being outside this range or having no transition at all down to 30 mK. Secondary ion mass spectroscopy (SIMS) analysis of a few films indicated some iron contamination at the interface between the sapphire and iridium, probably from the heater during bakeout of the vacuum

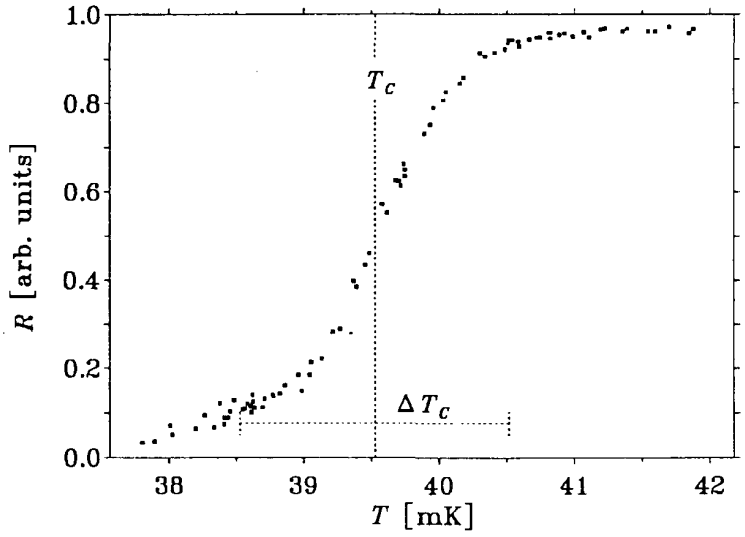

Fig. 1: The transition of a bilayer with the critical temperature $T_c = 39.5\,\mathrm{mK}$ and the transition width $\Delta T_c = 2\,\mathrm{mK}$.

system. This contamination could lower the critical temperature of the iridium films as superconductivity is very sensitive to ferromagnetic impurities. We include in this paper the data of runs in which the T_{cs} of the diagnostic iridium film was between 90 and 120 mK and its transition width ΔT_{cs} was less than 15 mK. We also include the runs where the iridium of the bilayer was evaporated on top of the gold, and is expected to be of better quality than the diagnostic iridium film deposited onto the room temperature substrate; for these runs we assume $T_{cs} = 112.5\,\mathrm{mK}$ in the further analysis.

The thickness d_s of our Ir films was varied between 700 Å and 4000 Å and the gold thickness d_n between 300 Å and 1100 Å. The lowest measured critical temperature of a bilayer was 33 mK and the steepest transition was 0.2 mK wide. A typical transition curve is plotted in Fig. 1.

3. COMPARISON WITH THEORY

Various theories which have been proposed to describe the proximity effect have been reviewed together with the data.[3–6] The theory for dirty films, where the electron mean free path ℓ is small compared to the coherence length $\ell \ll \xi$ was formulated by de Gennes and Guyon[7] and Werthamer.[8,9] It is not clear whether this theory should apply to our data, for which in some cases $\ell \sim d$. Ashida, *et al.*[6,10] have developed a theory for the clean limit, including also the reflection coefficient at the interface between the superconductor and the normal metal. However they have not compared their calculations to experimental results due to insufficient data on the Fermi velocities and the reflection coefficient. In the following we compare our data to the de Gennes-Werthamer theory.

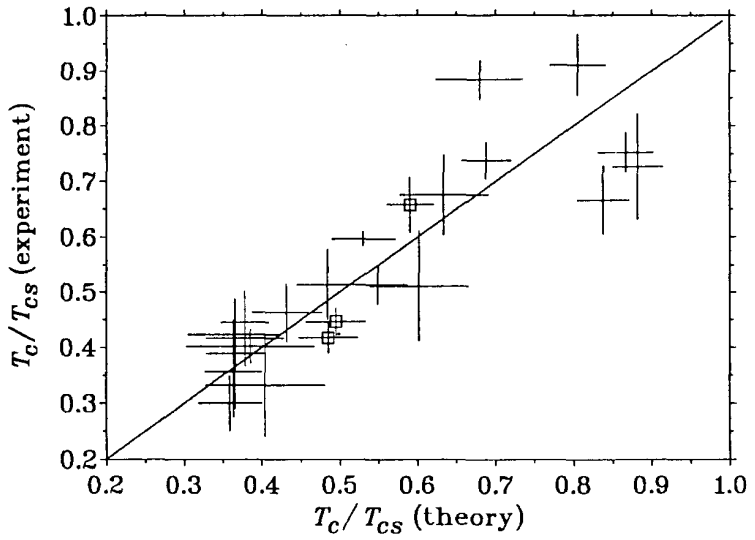

Fig. 2: Comparison of the experimental values of T_c/T_{cs} with those predicted by the modified theory with $\alpha = 0.2$. The squares correspond to the bilayers with the iridium film evaporated on the top of gold.

Werthamer[8,9] obtains a set of three coupled equations relating the critical temperature T_c of the bilayer and the characteristic lengths k_s and k_n to the effective coherence lengths ξ_s and ξ_n of Cooper pairs, the thicknesses d_s and d_n of the layers, and the critical temperatures T_{cs} and T_{cn} of the superconductor s and the normal metal n, respectively. For the case of gold, $T_{cn} \approx 0$ and one of the equations reduces to $k_n = 1/\xi_n$. The other two equations are then

$$\ln(T_{cs}/T_c) = \chi(\xi_s^2 k_s^2), \quad \text{and} \tag{1}$$

$$\left[N\xi^2 k \tan(kd)\right]_s = \left[N\xi \tanh(d/\xi)\right]_n \ . \tag{2}$$

Here $\chi(Z) \equiv \psi(\frac{1}{2} + \frac{1}{2}Z) - \psi(\frac{1}{2})$ and ψ is the digamma function. The density N of electronic states for one spin direction on the Fermi surface is proportional to the coefficient γ of the normal electronic specific heat: $\gamma = (2/3)\pi^2 k_B^2(1+\lambda)N$, where k_B is Boltzmann's constant, and λ is the electron-phonon coupling constant. The effective coherence lengths are given by[9]

$$\xi_{s,n} = \left[\sqrt{\frac{\pi\hbar k_B}{6T_c e^2 \gamma \rho}}\right]_{s,n},$$

where e is the electron charge, $\hbar$ is Planck's constant divided by 2π, and ρ is the low temperature resistivity. We used $\rho = \rho_{bulk}/RRR$, where ρ_{bulk} is the literature value of the bulk resistivity at room temperature.

We calculated the reduced critical temperature T_c/T_{cs} by solving Eqns. (1) and (2) numerically. The resulting T_c's were about a factor of two too high for films with measured $T_c/T_{cs} \sim 0.3$. The de Gennes-Werthamer theory has also been seen to give too high values of T_c for very thin Nb-Cu[5] and Nb-Al[11] multilayers.

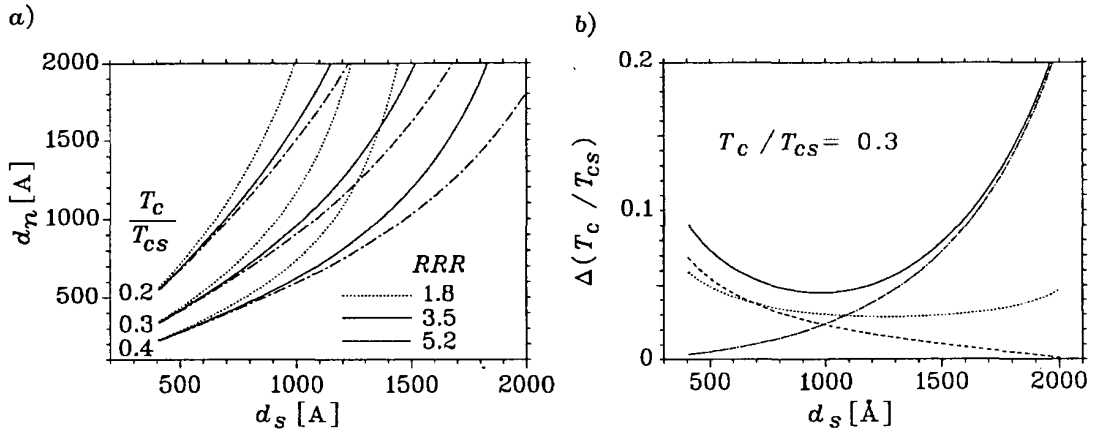

Fig. 3: *a*: Expectation from modified theory for the Au film thickness d_n needed to achieve $T_c/T_{cs} = 0.2$, 0.3 and 0.4 as a function of the thickness d_s of the Ir film. The calculation is done for various values of the RRR of the Ir film: $RRR = 3.5$ (solid line), $RRR = 1.8$ (dotted), $RRR = 5.2$ (dashed-dotted). *b*: The expected variation $\Delta(T_c/T_{cs})$ in the reduced critical temperature of an Ir-Au bilayer with $T_c/T_{cs} = 0.3$ using our average $RRR = 3.6$. The dotted line is the contribution of $\Delta d_s = 50$ Å, the dashed line that of $\Delta d_n = 50$ Å, and the dashed-dotted line that of our standard deviation $\Delta RRR = 1.0$. The solid line is the square root of the sum of the squares of these three errors.

We find that modifying the theory by replacing N_s with αN_s in (2), where α is a free parameter, gives a good fit to our data for $\alpha \approx 0.2$. The result is shown in Fig. 2. The error bars are calculated from the measurement errors combined in quadrature. For the experimental T_c/T_{cs} the errors in T_c and T_{cs} are taken to be half the widths of the corresponding transitions. The errors of the theoretical predictions of T_c/T_{cs} include the errors in the two thicknesses and the 3 % error in RRR. The bilayers with the iridium film evaporated on the top of gold are also seen to agree well with the modified theory.

In order to find suitable parameters to reliably produce bilayers with a desired T_c we have investigated the dependence of T_c on the various parameters as given by the modified model. Our gold films are thin compared to their effective coherence length $d_n/\xi_n \ll 1$ and the right-hand side of Eq. (2) reduces to $[Nd]_n$, i.e. the dependence on ξ_n cancels. Thus our T_c's do not depend on the RRR of the gold films. Fig. 3*a* shows the d_n needed to obtain $T_c/T_{cs} = 0.2$, 0.3, and 0.4 as a function of d_s. The different line types correspond to different values of the RRR of the iridium film. Fig. 3*b* shows the contribution of the errors $\Delta d_n = 50$ Å, $\Delta d_s = 50$ Å and $\Delta RRR = 1.0$ to the reproducibility of the reduced critical temperature of a bilayer with $T_c/T_{cs} = 0.3$. The minimum in the total error occurs at $d_s \approx$ 1000Å. This is near the region where we have four films produced under similar conditions ($d_s = 1260 \pm 75$ Å, $d_n = 1030 \pm 50$ Å, $RRR = 3.4 \pm 0.4$); they have critical temperatures $T_c = 37 \pm 4$ mK.

4. CONCLUSIONS

We have succeeded in producing superconducting phase transition thermometers working in the temperature range between 30 mK and 100 mK, which is not accessible with pure superconductors. The critical temperature of an Ir-Au bilayer can be calculated from the corresponding film thicknesses and the residual resistivity ratio of the superconductor film using the theory of de Gennes-Werthamer with the addition of one adjustable parameter.

Accurate film thickness control during the evaporation is necessary for controlling the T_c of the bilayer. The variation of T_c due to the changes of the effective coherence length could be reduced further by using thinner films.

Bilayers with iridium evaporated on top of gold are very promising. They have narrow transitions and the low substrate temperature ($T \leq 150\,°C$) during the deposition may allow the use of substrates other than sapphire as well as the use of photolithography lift-off techniques to produce bilayers with better-defined edges.

An energy resolution of 220 eV (FWHM) for 6 keV X-rays has recently been obtained in a 31 g sapphire crystal with an Ir-Au thermometer operated at 44 mK.[1]

ACKNOWLEDGMENTS

We are very grateful to Prof. H. Kinder for allowing us to use the Alpha-Step for film thickness measurement. We also thank the workshop of the Max-Planck-Institute for their support.

REFERENCES

1. M. Frank *et al.*, these proceedings.
2. A.D. Misener, J.O. Wilhelm, Trans. Roy. Soc. Can. 29, 1 (1935).
3. G. Deutscher and P.G. de Gennes, Superconductivity, Vol. II, ed. R.D. Parks. Marcel Dekker, Inc., New York (1969).
4. A. Gilabert, Annales de Physique 2, 203 (1977).
5. I. Banerjee, Q.S. Young, C.M. Falco, I.K. Shuller, Solid State Comm. 41, 805 (1982).
6. M. Ashida, J. Hara, K. Nagai, Phys. Rev. B 45,828 (1992).
7. P.G. de Gennes, E. Guyon, Phys. Lett. 3, 168 (1963).
8. N.R. Werthamer, Phys. Rev. 132, 2440 (1963).
9. J.J. Hauser, H.C. Treuerer, N.R. Werthamer, Phys. Rev. 136, A634 (1964).
10. M. Ashida, S. Aoyama, J. Hara, K. Nagai, Phys. Rev. B 40, 8673 (1989).
11. E. Liebemann, Physikalische Eigenschaften von Al/Nb-Multischichten. PhD thesis, University of Konstanz, Germany, 1991.

Signal to Noise Ratio of Superconducting Tunnel Junction Detectors

J.Jochum, H.Kraus, M.Gutsche, and B.Kemmather

Technische Universität München, Physik Department E15, 85748 Garching, Germany

The optimal signal to noise ratio for detectors based on superconducting tunnel junctions (STJ) is compared for the cases of a detector consisting of one single STJ, as well as of series and of parallel connections of STJs. A single STJ exhibits the best signal to noise ratio if the signal charge is independent of detector area. If signal charge increases in proprotion to the detector area, a parallel or a series connection of STJs would provide the optimum signal to noise ratio. The signal to noise ratio is deduced as function of junction parameters.

PACS numbers: 29.40, 29.60, 06.70

I. INTRODUCTION

The energy resolution of the STJ detectors is at present limited by electronic noise [1]. We shall investigate the dependence of electronic noise on detector parameters such as capacitance, resistance, quasiparticle life time and tunneling time.

Most applications require larger sensitive detector areas than those attained with prototype STJs during earlier experiments. In efforts to combine larger signal to noise ratios and large detector areas, we consider series and parallel arrays of STJs. We call these detectors: series or parallel STJ detectors.

II. SIGNAL TO NOISE RATIO

Absorption of energy yields free charge carriers, so called 'quasiparticles', created by Cooper pair breaking in the superconducting films of the detector. A fraction Q_t of the initial charge Q_0 causes the detector signal by tunneling of the quasiparticles in the junctions. The signal and the noise at the preamplifier output are described by $Q_tS(\omega)$ and by the spectral density $\mathcal{N}(\omega)$. The accuracy of energy measurement is determined by the ratio $\mathcal{R}_{sn}$ between signal height and noise. The amount of charge leading to a signal to noise ratio of $\mathcal{R}_{sn} = 1$ is called the 'equivalent noise charge' Q_n. The highest signal to noise ratio is achieved by application of the 'optimum filter' and is given by [2]:

$$\mathcal{R}_{sn}^2 = \frac{Q_t^2}{2\pi}\int_{-\infty}^{\infty}\frac{S^2(\omega)}{\mathcal{N}(\omega)}d\omega, \qquad Q_n = \frac{Q_t}{\mathcal{R}_{sn}} \tag{1}$$

The signal $Q_tS(\omega)$ is given by the product of $P(\omega)$, the transfer function of the

Presented at the Fifth International Workshop on Low Temperature Detectors (LTD-5), 29 July - 3 August 1993, Berkeley, California. To be published in Journal of Low Temperature Physics. An extended version of this paper is accepted for publication in NIM.

preamplifier and $I_t(\omega)$, the Fourier transform of the tunnel current given by:

$$I_t(\omega) = \frac{Q_t}{1 + i\omega\tau_p} \quad \text{with} \quad Q_t = \frac{\tau_p}{\tau_t} Q_0. \tag{2}$$

τ_t is the tunneling time and τ_p is the pulse length given by the effective decay time of quasiparticles in the films of a tunnel junction [3].

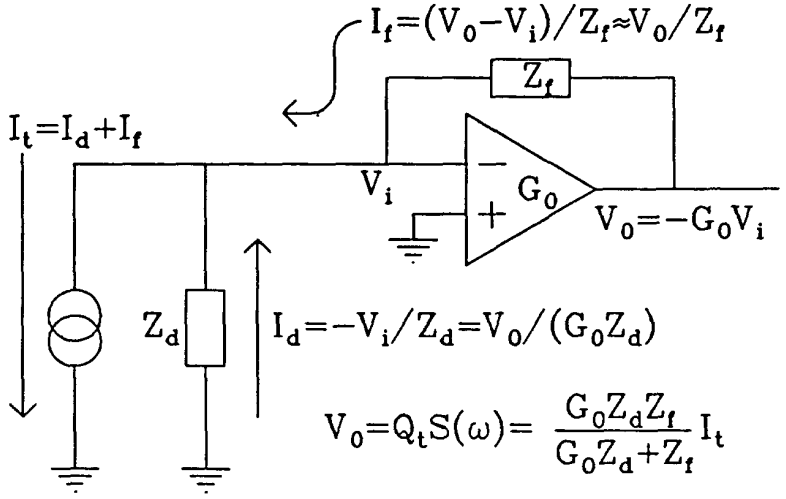

Fig.1: In a single or a parallel STJ detector, the entire detector acts as source of a signal current I_t. I_t is split into I_d and I_f flowing through the detector and the preamplifier, respectively. The preamplifier transfer function corresponds to the impedance $P(\omega)$ which, when multiplied by the signal current, yields the signal voltage at the preamplifier output.

The transfer function $P(\omega)$ of the preamplifier loaded with the impedance $Z_i(\omega)$ is given by

$$P(\omega) = \frac{G_0 Z_i(\omega) Z_f(\omega)}{G_0 Z_i(\omega) + Z_f(\omega)} \tag{3}$$

$Z_f(\omega)$ and G_0 are the feedback impedance of the preamplifier and its open loop gain. In a charge sensitive preamplifier, $Z_f(\omega)$ consists of a capacitance C_f in parallel with a resistance R_f. The impedance $Z_i(\omega)$ includes the detector impedance $Z_d(\omega)$, the gate capacitance C_g of the input FET, and additional parasitic capacitances in parallel. In case of a single STJ detector its impedance consists of the junction capacitance C_j in parallel with the dynamical resistance R_j. In general, the detector impedances $Z_d(\omega)$ are $Z_j(\omega), Z_j(\omega)/M$ and $MZ_j(\omega)$ for a single, parallel, and series STJ detector, respectively.

The signal current I_t arises from the junction in which energy is absorbed. Consequently, for a single or a parallel STJ detector (Fig.1), the signal current source is located across the entire detector whereas in the case of a series STJ detector (Fig.2) it appears across the impedance of the energy absorbing tunnel junction only. The signal $Q_tS(\omega)$ in these cases is

$$Q_tS(\omega) = \begin{cases} P(\omega)I_t(\omega), & \text{single or parallel STJ detector,} \\ \frac{1}{M}P(\omega)I_t(\omega), & \text{series STJ detector with M junctions.} \end{cases} \tag{4}$$

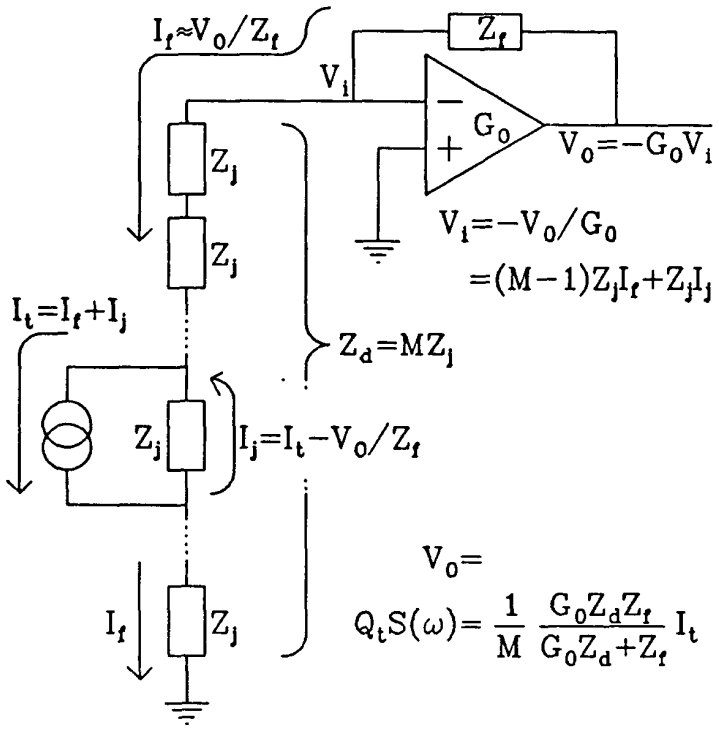

Fig.2: In a series STJ detector only the junction where energy absorption occurs acts as source of the signal current, which is split into I_j flowing through this particular tunnel junction and I_f flowing through the preamplifier and the other junctions of the detector. A factor 1/M, compared to the case in Fig.1, arises in the calculation of the output signal, since the total detector impedance $Z_d(\omega) = MZ_j(\omega)$ enters into the transfer function.

The various noise sources are shown in Fig.3. The series noise **a** is caused by the thermal noise in the channel of the input FET. The parallel noise **b**, is caused by the thermal noise of the resistors in the circuit, the shot noise of the detector bias current and the gate leakage current of the input FET. An additional contribution to the series noise is 1/f noise described by $\mathbf{c}/|\omega|$. The total noise power spectrum at the preamplifier output is given by

$$\mathcal{N}(\omega) = \left\{ \mathbf{b} + (\mathbf{a} + \frac{\mathbf{c}}{|\omega|})(\frac{1}{R_i^2} + \omega^2 C_i^2) \right\} P^2(\omega), \quad C_i \approx C_d || C_g, \; R_i \approx R_d \qquad (5)$$

The optimal signal to noise ratio resulting from signal (4) and noise (5) is

$$\mathcal{R}_{sn} = Q_t \left\{ \frac{1}{\pi K^2 \mathbf{b_a}} \int_0^\infty \frac{d\omega}{(1+\omega^2\tau_s^2 + \frac{\mathbf{c}}{\mathbf{a}\omega}\rho^2(1+\omega^2\tau_{det}^2))\,(1+\omega^2\tau_p^2)} \right\}^{\frac{1}{2}}, \quad Q_n = \frac{Q_t}{\mathcal{R}_{sn}}$$

$$\text{with} \quad \mathbf{b_a} = \mathbf{b} + \frac{\mathbf{a}}{R_d^2}, \quad \tau_s = \sqrt{\frac{\mathbf{a}}{\mathbf{b_a}}}\, C_i, \quad \tau_{det} = R_d C_i, \quad \rho = \sqrt{\frac{1}{1 + \frac{\mathbf{b}}{\mathbf{a}} R_d^2}} \qquad (6)$$

The number of the elements connected in series is K = 1 for a single or a parallel STJ detector and K = M for a series STJ detector of M elements. For a CR-RC

shaper with equal time constants for integration and differentiation τ_s represents the optimal shaping time in the case of a charge sensitive preamplifier and for $\tau_s \gg \tau_p$ [4]. For our tunnel junction detectors $\tau_s \lesssim \tau_p$ applies, and thus the influence of τ_p on the signal to noise ratio must be taken into account. A low value of R_d increases the contribution of the effective parallel noise $\mathbf{b_a}$. The parameter ρ $(0 < \rho \leq 1)$ describes the influence of the detector resistance R_d on effective parallel noise $\mathbf{b_a}$ and on the contribution of 1/f noise. A value for ρ, small enough to neglect 1/f noise can be achieved, whence we shall disregard 1/f noise in the following.

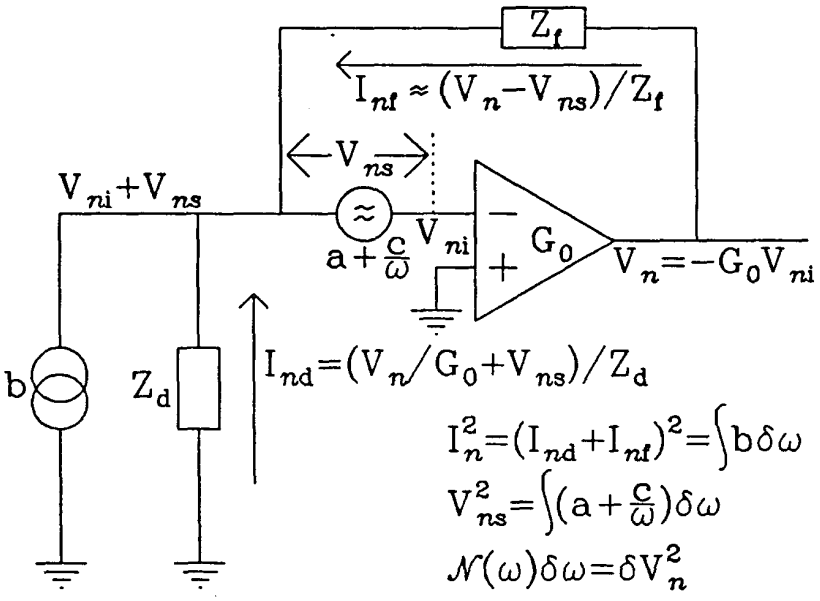

Fig.3: The noise current in parallel to the signal current resulting from thermal noise of bias and feedback resistors and from shot noise of bias and FET-gate leakage currents is described by the spectral power density $\mathbf{b}$. The thermal noise in the FET-channel is equivalent to a noise voltage at the FET-gate in series with the detector. This white series noise added to the 1/f noise of the input FET is denoted by the spectral power density $\mathbf{a} + \mathbf{c}/\omega$.

According to equation (6) the optimal signal to noise ratio $\mathcal{R}_{sn}$ and the equivalent noise charge Q_n, neglecting 1/f noise, are given by

$$\mathcal{R}_{sn} = Q_t/Q_n \qquad \text{with} \quad Q_n = K \cdot \sqrt{2b_a(\tau_s + \tau_p)} = K \cdot \sqrt{\sqrt{4ab_a}C_i + 2b_a\tau_p} \qquad (7)$$

The first term of Q_n under the square root $(2b_a\tau_s)$ can be interpreted as the noise charge collected during the optimal shaping time τ_s. The second term $(2b_a\tau_p)$ is associated with the additional noise charge generated by the effective current noise during the time τ_p required for the collection of the signal charge. We shall call them the FET noise term $(2b_a\tau_s)$ and the pulse noise term $(2b_a\tau_p)$. At present for our tunnel junction detectors $\tau_s \lesssim \tau_p$ applies and the pulse noise term is somewhat larger than the FET noise term.

To asses the noise charges Q_n for different detector types, the dependence of the values $\mathbf{a}$, $\mathbf{b_a}$, $\mathbf{c}$, C_i, and τ_p on the detector type has to be determined:

Pulse length τ_p: τ_p depends on quasiparticle life time and tunneling time and thus on the purity of the materials and on the quality of the tunnel barrier. Both are independent of detector type, implying equal pulse lengths for single, series, and parallel STJ detectors.

White series noise constant a: For a JFET **a** is given by

$$\mathbf{a} = 2kT \cdot 0.65/g_m \quad \propto 1/C_d \tag{8}$$

T, k, and g_m are the temperature of the FET, the Boltzmann constant, and the FET forward transconductance, respectively [5]. g_m is proportional to the gate capacitance C_g. In order to minimize the FET noise term, the gate capacitance C_g of an FET has to be equal to the detector capacitance C_d. For a properly matched FET the series noise **a** then becomes inversely proportional to C_d

Input capacitance C_i: $C_i \approx C_d + C_g$. FET matching yields $C_i = 2C_d$.

1/f noise constant c: The constant **c** depends on the gate capacitance in the same way as constant **a** [6]. For the case of CR-RC shapers having equal time constants for differentiation and integration, 1/f noise contribution is likewise minimized by the condition $C_g = C_d$ [7]. Hence, for an FET capacitively matched the 1/f noise constant is also inversely proportional to C_d.

Parallel noise constant b: By lowering the operating temperature T of the feedback resistor, the bias resistor, and the input FET, the parallel noise is eventually dominated by the shot noise of the detector bias current

$$\mathbf{b} = eI_b \tag{9}$$

Provided tunnel junctions are equal, each of them requires the same bias current I_b. Hence, a detector consisting of M STJs connected in parallel requires a bias current MI_b and its parallel noise constant is M times larger than that for a single STJ detector. M series connected STJs have to be biased with the current I_b of a single junction. Thus, a shot noise $\mathbf{b} = eI_b$ arises in parallel to each junction in the same way as the signal current in Fig.2. The corresponding noise power density at the preamplifier output is proportional to eI_b/M^2 (cf.(4)). As there are a number of M such noise current sources, a noise power density proportional to eI_b/M results. Compared to a single STJ, the parallel noise constant of M series connected STJs is therefore reduced by a factor M.

We shall now evaluate the equivalent noise charges Q_n for the different detector types. The quantities $\mathbf{a_j}$ and $\mathbf{b_{aj}}$ denote the values of a single 'normal sized' tunnel junction detector specified by the index j. C_j, R_j are the capacitance and the dynamical resistance of a 'normal sized' tunnel junction, respectively. With the help of equation (7) and the above remarks, the minimal equivalent noise charges for the different detector types are compared:

$$Q_n = \begin{cases} \sqrt{\sqrt{4\mathbf{a_j}\mathbf{b_{aj}}}\, 2C_j + 2\mathbf{b_{aj}}\tau_p} & = Q_{nj}, \quad \text{single junction} \\ \sqrt{\sqrt{4\mathbf{a_j}\mathbf{b_{aj}}}\, 2MC_j + 2M\mathbf{b_{aj}}\tau_p} & = \sqrt{M} \cdot Q_{nj}, \quad \text{parallel connection} \\ M\sqrt{\sqrt{4\mathbf{a_j}\mathbf{b_{aj}}}\, 2\frac{C_j}{M} + 2\frac{\mathbf{b_{aj}}}{M}\tau_p} & = \sqrt{M} \cdot Q_{nj}, \quad \text{series connection} \end{cases} \tag{10}$$

Since the equivalent noise charges Q_n are calculated under optimal conditions, they represent the lowest possible limits. The lowest equivalent noise charge Q_n is obtained for a single STJ detector.

The parallel and series connections of M STJs exhibit noise charges which are in both cases larger by a factor of $\sqrt{M}$.

The reduced equivalent noise charge for a smaller detector capacitance was often considered as a possibility to increase the signal to noise ratio by connecting many STJs in series. A direct proportionality of Q_n to the detector capacitance C_d ($Q_n \propto C_d$) only holds, if series noise **a** dominates as a consequence of incorrectly adjusted shaping time constant. But also in such a case, the signal to noise ratio would not be enhanced for series STJs. In a charge sensitive measurement, the equivalent noise charge is reduced for series STJs compared to a single STJ, but also is the the signal charge transferred into the preamplifier. In a voltage sensitive measurement the signal voltage as well as the noise voltage at the preamplifier output remain the same for the two detector types. If the signal of a voltage measurement is mixed up with the noise of a charge measurement, a better signal to noise ratio for series STJs is incorrectly deduced!

The best signal to noise ratio is obtained in the case of a single STJ detector, if the amount of energy deposited is independent of detector size, e.g. in the case of X-ray detection. A different situation arises, if the amount of energy detected increases in proportion to the sensitive area of a tunnel junction detector, e.g. in the case of phonon detection [8,9]. In this situation the signal charge Q_t is M times larger for parallel or series STJ detector than for a single STJ detector. The equivalent noise charges of parallel and series STJ detectors increase by a factor $\sqrt{M}$, whence the signal to noise ratios are enhanced by $\sqrt{M}$ relative to a single STJ detector. A detector with the same sensitive area but employing quasiparticle trapping, has the advantage of the low equivalent noise charge of a single STJ detector [1]. A trapping detector may be the best detector for phonon detection, especially if the FET matching for a series or parallel STJ detector turns out to be difficult.

To estimate qualitatively the effect of a non vanishing 1/f noise, we consider the signal to noise ratio given by equation (6). With an FET properly matched to the detector capacitance, the parameters τ_p, ρ, τ_s and the ratio of noise constants **c/a** are independent of detector type. The only term affected by the detector type then is $K^2\mathbf{b_a}$. One can easily visualize that the relations between the different equivalent noise charges do not change, even if 1/f noise is taken into account.

III. DEPENDENCE OF $\mathcal{R}_{sn}$ ON JUNCTION PARAMETERS

The ratio $\mathcal{R}_{sn}$ of a tunnel junction detector depends on the parameters of an individual tunnel junction. The influence of the junction parameters on signal to noise ratio, such as tunneling time, life time, etc. will be elucidated in this section.

Under the condition of optimal shaping, the contribution of electronic noise to the signal to noise ratio of a single STJ detector is given by

$$\mathcal{R}_{sn} = \frac{Q_t}{Q_n} = \frac{\frac{\tau_p}{\tau_t} Q_0}{\sqrt{2\mathbf{b_a}(\tau_s + \tau_p)}} \,. \tag{11}$$

The pulse length τ_p affects <u>both</u> signal charge Q_t and equivalent noise charge Q_n. The influence of pulse length on the signal to noise ratio can be illustrated by considering 'back tunneling'. If quasiparticles stay confined to the tunnel area, they

have a chance to tunnel repeatedly and this way amplify the signal charge [10]. This situation is often referred to as 'back tunneling'. The pulse length τ_p is then determined by the quasiparticle life time τ_ℓ. On the contrary if quasiparticles would leave the tunnel area immediately once they have tunneled, the pulse length τ_p is shorter, involving both life time τ_ℓ and tunneling time τ_t:

$$\tau_p = \tau_\ell \quad \text{with back tunneling,} \qquad \tau_p = \frac{\tau_\ell \tau_t}{\tau_\ell + \tau_t} \quad \text{without back tunneling} \tag{12}$$

Back tunneling increases the signal charge Q_t by a factor g_{bt}

$$g_{bt} = 1 + \frac{\tau_\ell}{\tau_t} \tag{13}$$

This gain g_{bt} is due to a longer pulse length (12), rather than a higher current, giving at the same time rise to a higher noise charge. The gain G_{bt} associated with the signal to noise ratio is somewhat smaller:

$$g_{bt} > G_{bt} > \sqrt{g_{bt}} \tag{14}$$

If the noise charge is dominated by the pulse noise term ($2\mathbf{b_a}\tau_p$), only the square root of the signal charge gain g_{bt} enters in the signal to noise ratio $G_{bt} = \sqrt{g_{bt}}$.

Back tunneling on the one hand maximizes the signal to noise ratio, while on the other hand it limits the maximum counting rate. We will nevertheless assume in the following the presence of back tunneling.

The series noise **a** for a properly matched FET is inversely proportional to the capacitance C_j of the tunnel junction and hence to the tunnel area A_t.

The ratio $Q = R_j/R_{nn}$ between dynamical resistance R_j and the normalconducting resistance R_{nn} (at voltages $V_b \gg 2\Delta/e$) is an indicator of STJ quality whence we call Q the 'quality factor'. The normalconducting resistance R_{nn} is proportional to the tunneling time τ_t of quasiparticles and is inversely proportional to the tunnel area A_t. Hence, the dynamical resistance of a tunnel junction is

$$R_j \propto Q\tau_t/A_t \tag{15}$$

At the usual low operating temperatures, the bias current of our STJ detectors is caused by imperfections of the tunnel barrier and of the film quality. The bias current is then inversely proportional to the dynamical resistance R_j of a tunnel junction [11]. Consequently we obtain for the parallel noise

$$\mathbf{b} \propto A_t/\ Q\tau_t, \tag{16}$$

Eventually, four parameters are decisive for the contribution of electronic noise to the signal to noise ratio of a STJ detector: the quasiparticle life time τ_ℓ, the tunneling time τ_t, the quality factor of the tunnel junction Q, and the tunnel area A_t. We obtain for the signal to noise ratio

$$\mathcal{R}_{sn} = \begin{cases} \frac{Q_t}{\sqrt{2\mathbf{b}\tau_p}} \propto \sqrt{\frac{Q\ \tau_\ell}{A_t\tau_t}}, & \text{if pulse noise term dominates, } \tau_p \gg \tau_s \\ \frac{Q_t}{\sqrt{2\mathbf{b}\tau_s}} \propto \tau_\ell\sqrt{\frac{\sqrt{Q}}{A_t\tau_t\sqrt{\tau_t}}}, & \text{if FET noise term dominates, } \tau_p \ll \tau_s. \end{cases} \tag{17}$$

To reduce electronic noise, a high quality factor Q, a short tunneling time τ_t, and a long life time τ_ℓ are essential. If the tunnel area A_t is enlarged, the detector

capacitance and consequently the FET noise term increases. Simultaneously the dynamical resistance reduces requiring a higher bias current and thus leads to a higher effective parallel noise. In both cases the signal to noise ratio is proportional to $1/\sqrt{A_t}$, necessitating small tunnel areas. On the contrary there exist lower limits for the tunnel junction size due to the quasiparticle pair recombination, which would lead to a non linear energy response of the detector [3].

IV. SUMMARY

The signal to noise ratio, which can be achieved under optimal conditions such as bias and feedback resistors operated at low temperatures, an input FET matched to the detector, and optimal pulse shaping, was compared for the cases of a single STJ and a parallel or a series connection of M STJs. For a fixed signal charge, as prevailing in the case of X-ray detection, a single STJ detector yields the best signal to noise ratio. The ratio becomes worse by a factor $\sqrt{M}$ for a parallel or series connection of M STJs compared to a single STJ. If the signal charge increases in proprotion to the sensitive area, as in the case of phonon detection, a parallel or series STJ detector or a trapping detector are the better choices.

Back tunneling increases the signal charge but at the same time increases also the noise charge to some extent. The gain in signal to noise ratio by implementation of back tunneling is smaller than anticipated by the gain in signal charge alone.

To maximize the signal to noise ratio, a long quasiparticle life time τ_ℓ, a short quasiparticle tunneling time τ_t, a high quality factor Q, and a small tunnel area A_t are essential. Under the conditions prevailing in our experiments, the signal to noise ratio depends on the square root of all these parameters.

This work is supported by the Bundesministerium für Forschung und Technologie.

REFERENCES

[1] H.Kraus, F.v.Feilitzsch, J.Jochum, R.L.Mössbauer, Th.Peterreins, F.Pröbst, Phys.Lett.B 231, 1989, p.195
[2] E.Gatti and P.F.Manfredi, 'Processing the signals from solid-state detectors in elementary-particle physics', La Rivista del Nuovo Cimento, vol.9,ser.3, 1986
[3] J.Jochum, H.Kraus, M.Gutsche, B.Kemmather, F.v.Feilitzsch, R.L.Mössbauer 'Dynamics of ...', submitted for publication to Annalen der Physik
[4] M.Tsukuda, Nucl.Instr.Meth. 14, 1961, p.241
[5] R.S.C.Cobbold, 'Theory and applications of FET's', Wiley Intersc., N.Y., 1970
[6] P.O.Lauritzen, Solid State Electronics, 8, 1965, p.41
[7] E.Kowalski, 'Nuclear Electronics',Springer-Verlag, Berl.-Heidelb.-N.Y., 1970
[8] T.Peterreins, J.Jochum, F.Pröbst, F.v.Feilitzsch, H.Kraus,R.L.Mössbauer, J.Appl.Phys.,69(4), 1991, p.1791
[9] D.J.Goldie in Proceedings of 'X-ray Detection by Superconducting Tunnel Junctions', ed. A.Barone, R.Cristiano,S.Pagano, World Scn., Singp.1991, p.98
[10] F.Pröbst, H.Kraus, T.Peterreins, F.v.Feilitzsch, N.I.M. A 280, 1989, p.251
[11] H.Kraus, J.Jochum, B.Kemmather, M.Gutsche, F.v.Feilitzsch,R.L.Mößbauer, in 'EUV, X-Ray, and Gamma-Ray Instrumentation for Astronomy III', ed. O.H.W.Siegmund, Proc. SPIE 1992, p.1743

Photolithographic Fabrication of Tunnel Junction Detectors

B. Kemmather, H. Kraus, J. Jochum, and M. Gutsche

Technische Universität München, Physik Department E 15, 85748 Garching, Germany

The complex structure in present state of the art superconducting tunnel junction detectors requires photolithographic production of the detector layout. With such a technique we achieve an edge definition better than 2μm. Lift off processes proved to be beneficial in the fabrication of high quality tunnel junctions. In addition we have investigated multilayer structures of insulators with backsloping edges. The combination of both techniques allows us to produce the tunnel junction within a single vacuum cycle.

PACS numbers: 29.40, 81.15 G

INTRODUCTION

In earlier experiments we have used shadow mask techniques to define the structures of the detector elements such as absorber, tunnel junction layers, and protective coatings. Thus, it was possible to fabricate the entire detector within one vacuum cycle. However, the drawback of this method was that the definition of the structures was limited to an accuracy of worse than 15 μm. In addition, epitaxial growth and the application of masks is incompatible. The present generation of detectors with epitaxial absorbers, small tunnel junctions with a high aspect ratio, and quasiparticle trapping required the introduction of photolithographic methods.

DETECTOR FABRICATION

Epitaxial vanadium absorber films are grown in an ultra high vacuum system. The base pressure during the deposition process is in the 10^{-11} mbar range, except for hydrogen with $\sim 10^{-10}$ mbar. Single cristalline vanadium is evaporated with a $2kW$ e-gun and deposited on glass, Al_2O_3, or MgO substrates at different substrate temperatures up to $950°C$. The best result up to now is a vanadium film grown on MgO at a substrate temperature of $535°C$, which exhibits a mean free path for electrons of $\sim$ 6400Å.

The absorber is patterned using a standard photolithographic process and a wet etch bath is applied to remove the unwanted parts of the vanadium. The absorbers produced this way have a size of $\sim 140\mu m \times 500\mu m$ and a thickness of $\sim$ 2000 Å.

Presented at the Fifth International Workshop on Low Temperature Detectors (LTD-5), 29 July - 3 August 1993, Berkeley, California. To be published in Journal of Low Temperature Physics.

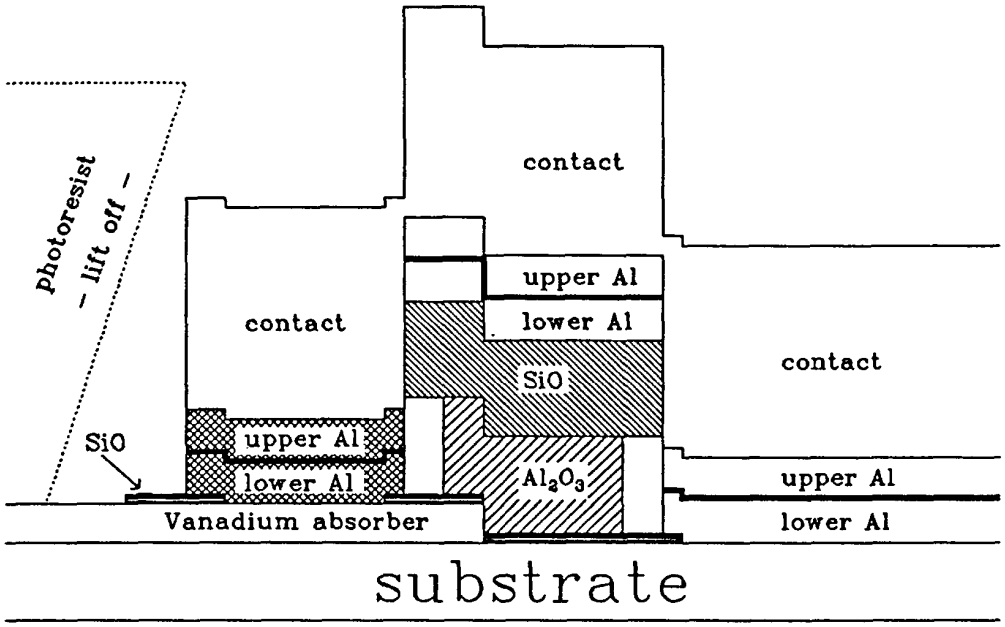

Fig. 1. Schematic cross section of the detector. Shaded: Table-structure. Criss-crossed: Tunnel junction. A detailed description is given in the text.

During the next step, a photolithographic lift-off structure is fabricated defining windows through which the lower films of the tunnel junctions have close contact with the absorber. A SiO layer of thickness $\sim$ 200 Å is evaporated. With the help of such a SiO window contact of the upper film of the tunnel junction to the absorber is avoided (see fig. 1).
Next, a 'table-structure', consisting of a lower Al_2O_3 and an upper SiO layer , is produced. Both layers are defined by one photoresist lift-off structure. After removal of the photoresist, the Al_2O_3 is selectively wet etched. The purpose of the 'table-structure' is to disrupt electrical contact across one of its edges during fabrication of the tunnel junction (lower AL and, upper Al, sperated by an oxide barrier)

To produce the tunnel junctions and their individual contact pads within one vacuum cycle, another lift-off structure is now applied. Prior to the deposition of the tunnel junctions, the absorber has to be cleaned with a low energy argon plasma to remove native oxides and other contaminants. This is done in a load lock attached to the main vacuum chamber. The aluminum layers of the tunnel junctions are evaporated using an e-gun. The pressure during film deposition is $\sim 10^{-7}$mbar. The lower aluminum layer has a thickness of $\sim$ 2000 Å and no electrical contact across the rim of the 'table'. The tunnel barrier is formed by oxidation with an oxygen plasma in the load lock and the upper aluminum layer is deposited.
The last step is the deposition of the contact layer, thick enough not to be disrupted by the rim of the 'table-structure'. This way the tunnel junction layers and the contact pad are produced without breaking the vacuum. Thereafter the detector

is removed from the vacuum system and the unwanted parts of the structure are removed by washing away the lift-off photoresist, leaving tunnel junctions with a size of $\sim 100\mu m \times 100\mu m$ residing on the vanadium absorber.

SUMMARY

Our fabrication process enables us to produce high quality tunnel junctions. The current voltage characteristics of such a junction is shown in fig. 2. The edges of our structures are defined to better than $2\mu m$. The principal advantage of our process is that the tunnel junctions can be created within one vacuum cycle and that cleaning processes during critical phases are avoided. Mechanical shadow masks are now entirely unnecessary.

This work is supported by the Bundesministerium für Forschung und Technologie.

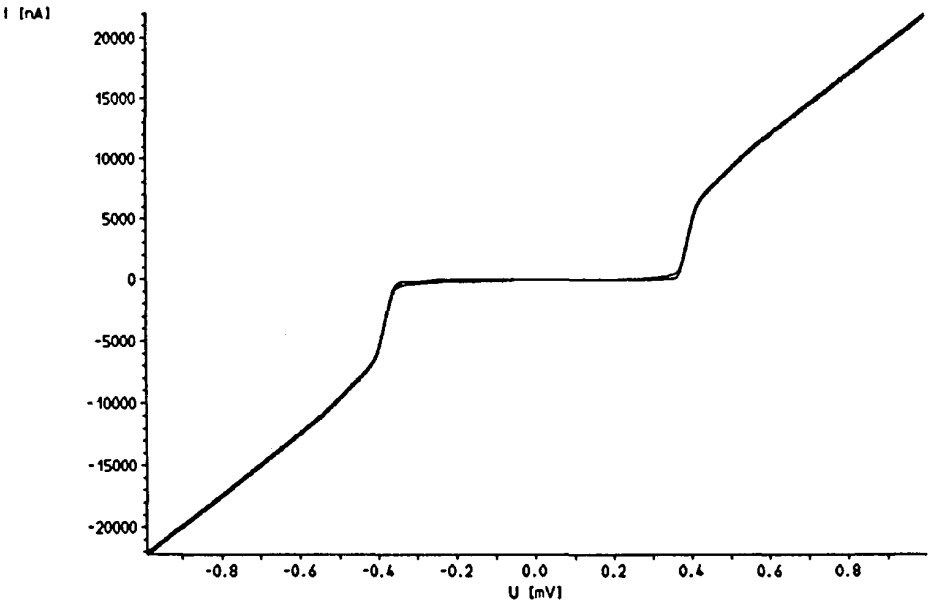

Fig. 2. Current voltage characteristic of a tunnel junction produced with the described process